123 Main Street
White Plains, New York 10601
914 681 6846

NewYork Power Authority

Ralph E. Beedle
Executive Vice President
Nuclear Generation

July 16, 1991
JPN-91-037

U.S. Nuclear Regulatory Commission
ATTN: Document Control Desk
Mail Station P1-137
Washington, D.C. 20555

SUBJECT: James A. FitzPatrick Nuclear Power Plant
Docket No. 50-333
Request for Additional Information -
Proposed Changes to the Technical Specifications
Spent Fuel Pool Storage Capacity (JPTS 90-035)

Reference: NRC letter, D.E. LaBarge to J.C. Brons, dated November 20, 1990, "Request No. 2 for Additional Information - Spent Fuel Pool Storage Capacity Increase."

Dear Sir:

The NRC requested additional information concerning the Authority's proposed changes to the FitzPatrick Technical Specifications for increased spent fuel storage capacity in the above reference. Attachment I provides the Authority's response. Attachment II is the Holtec Report HI-91614 which supports the Authority's response regarding the capability of DYNARACK computer code.

If you have any further questions, please contact Mr. J. A. Gray, Jr.

Very truly yours,

Ralph E. Beedle
Executive Vice President
Nuclear Generation

STATE OF NEW YORK
COUNTY OF WESTCHESTER

Subscribed and sworn to before me
this 16th day of July 1991.

Mina Holden

Notary Public

MINA HOLDEN
NOTARY PUBLIC, State of New York
Westchester County
No. 4629150
My Commission Expires Aug. 31, 1991

cc: see next page

A001
1/1

cc: Regional Administrator
U.S. Nuclear Regulatory Commission
475 Allendale Road
King of Prussia, PA 19406

Office of the Resident Inspector
U.S. Nuclear Regulatory Commission
P.O. Box 136
Lycoming, NY 13093

Mr. Brian C. McCabe
Project Directorate I-1
Division of Reactor Projects - I/II
U.S. Nuclear Regulatory Commission
Mail Stop 14 B2
Washington, D.C. 20555

RESPONSE TO NRC REQUEST 2 FOR ADDITIONAL INFORMATION SPENT FUEL POOL STORAGE CAPACITY INCREASE

NRC Question 1

P. 6-4. It is stated that "lift off of the support legs and subsequent liner impacts must be modelled using appropriate impact (gap) elements, and Coulomb friction between the rack and the pool liner must be simulated by appropriate precise [sic] linear springs."

Discuss, with specific examples, how one simulates Coulomb friction by appropriate piecewise linear springs. Demonstrate that such model does simulate actual physical responses by means of experimental data or analytical solutions. Provide a discussion of mathematical basis of such model which was utilized in your computer program and provide a simple calculation whereby one can compare with a closed form solution or an alternate numerical approach to establish the validity of your solution.

Supplement to NRC Question 1

During a phone conversation, the NRC agreed that the Authority could show that the relative sliding velocity between the rack pedestal and pool liner is "low" enough so that a constant coefficient of friction may be used, instead of responding to the third part of NRC Question 1.

NYPA Response:

Simulation of Coulomb friction by piecewise linear springs

The methodology for modeling Coulomb friction by piecewise linear springs in the FitzPatrick rack analysis was adopted from NYPA's Reference 1. Holtec Report HI-91614 (Attachment II) provides a specific example that shows the capability of DYNARACK to simulate frictional phenomena.

Model demonstration

The result of the rack analysis demonstrates that DYNARACK works. The mathematical basis of using such a model in the DYNARACK computer program is explained in detail in the response to NRC Question 2.

Relative Sliding Velocity

To determine the relative sliding velocity at the pedestal-liner interface, the Authority reviewed the results of one of the DYNARACK simulations. Specifically, the Authority examined the results from an analysis of the B rack (11x12). The net horizontal velocity of the pedestal base, relative to the floor was calculated as a function of time.

Figure 1 provides a plot of the net velocity V defined as:

$$V = (VX^2 + VY^2)^{1/2}$$

where VX, VY are the instantaneous velocity in the X and Y directions, respectively. Figure 1 shows that $V_{max} \approx 3.3$ in./sec, which the Authority considers "low". For such a "low" velocity, the variation in coefficient of friction will not be significant.

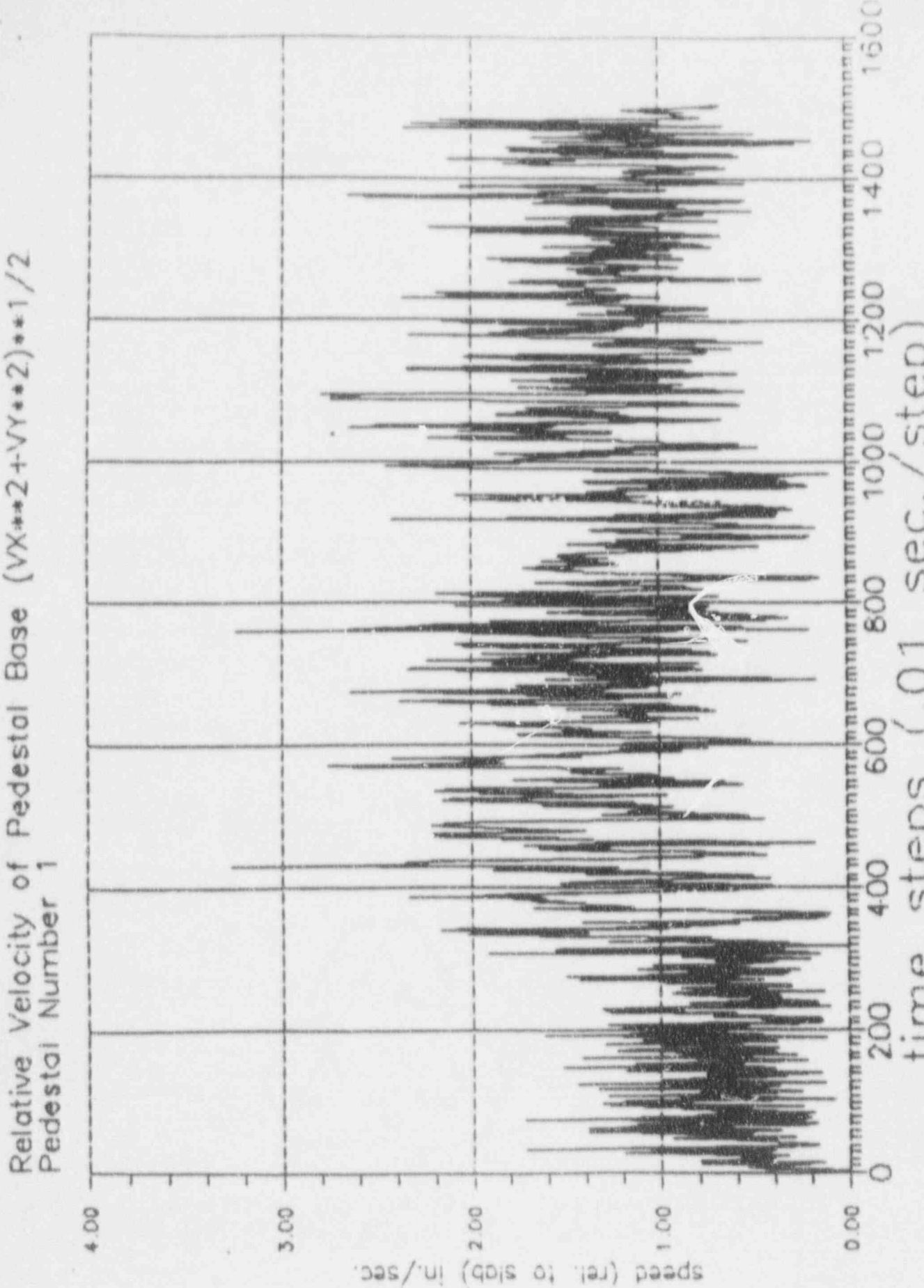
Relative Velocity of Pedestal Base (VX**2+VY**2)**1/2
Pedestal Number 1
speed (rel. to slab) in./sec.
4.00
3.00
2.00
1.00
0.00
0
200
400
600
800
1000
1200
1400
1600
time steps (.01 sec./step)

FIGURE 1

NRC Question 2

P. 6-15. It is stated that a central difference scheme is used for solution of the governing differential equations. Demonstrate how such a scheme can adequately depict various response phenomena, such as, subharmonic, bifurcation, and instability associated with nonlinear dynamics. Provide a specific example for such demonstration similar to that provided in references (1) and (2). Discuss how error associated with numerical integration is assessed and accounted for in a similar manner as that of reference (3). Also provide verification of the computer results with available experimental data.

NYPA Response:

Depicting response phenomena and using a specific example

Attachment II provides DYNARACK simulations using a central difference scheme to predict classical nonlinear phenomena such as subharmonics, bifurcation and instability. Specific examples similar to those provided in the NRC's References (1) and (2) are included in Attachment II. These nonlinear response phenomena associated with classical nonlinear dynamics, are not exhibited by the racks; however, the DYNARACK program has the capability of predicting these phenomena, if they occur.

Assessing and accounting for error associated with numerical integration

NYPA's Reference 1 provides an example of the stability and convergence properties of the central difference analyses. This example shows that the smaller the time step, the closer the solution approaches the "exact" solution. There is a certain critical time step above which the solution is unstable. In fact, to retain accuracy during the calculation, the time step should be as small as 0.31/W, where W is the highest linear natural frequency (rad./sec.). The result in NYPA's Reference 1 is modified by nonlinear effects and by damping, but generally there will be an upper limit for Δt dictated by stability and a lower limit dictated by round-off error.

NYPA's Reference 1 also shows that the time step for convergence will always be smaller than the time step for stability. Therefore, if the convergence requirements are met, stability will result.

To check the time step required for convergence, the Authority selected an analysis and ran it with different time steps to ensure that final conclusions concerning structural integrity and rack movement were correct. Holtec re-examined run CO2 from the licensing report (6x14 rack, full load of normal fuel, SSE, Coef. of friction = 0.8). Table 1 shows the results of runs with differing time steps. Results for top of rack displacements and pedestal stress factor R6 are compared. The critical stability upper limit on time step is between 0.00045 and 0.00049.

The time step used for single rack analysis in the licensing report was 0.00005 sec. This value is approximately one-tenth the stability limit and is also large enough to ensure that numerical round-off errors do not affect the results.

Table 1

6 X 14 SPENT FUEL RACK, NORMAL FUEL, S[illegible]
CONVERGENCE STUDY

Time Step (sec.)	DX (in.)	DY (in.)	R6 (max.)
.00049	RESULTS UNSTABLE - RUN ABORTED		
.00045	.3455	.0654	.272
.00040	.3488	.0621	.257
.00025	.3704	.0689	.290
.00010	.3872	.0630	.278
.00007	.3445	.0678	.300
.00005	.3826	.0626	.293
.00003	.3267	.0686	.259
.00002	.3824	.0677	.287
.00001	.3488	.0621	.257

Verifying computer results with available experimental data

The Authority has reviewed the references mentioned in NRC Question 2, as well as others for the existence of experimental data to permit numerical simulation and verification of computer results. The Authority was not able to locate sufficient information and provide a numerical verification of any experiments. Furthermore, the Authority believes that there has been no full scale testing of fuel racks in water subjected to 3-D seismic excitation that could be used as a benchmark.

NRC Question 3

P. 6-25. It is stated that "Plastic analysis is used to obtain the limiting impact load. The limit load is calculated as 4585 lbs. per cell which is much greater than the loads obtained from any of the simulations." Discuss how this statement may be translated into stress regime in fuel rods. Provide also the margin in terms of allowable stresses which exists in fuel rods.

NYPA Response:

The limit load of 4585 lbs per cell represents the ultimate load capacity of the rack cell. Actual rack-to-fuel impact loads are much smaller than 4585 lbs per cell.

The maximum instantaneous load is 339 lbs at the 1/4 elevation, or approximately at the second spacer location of the fuel assembly.

The seismic analysis of a single rack as discussed in Section 6.2 of the Licensing Report models the fuel assemblies in individual storage location as five (5) lumped masses, located at different levels of the rack. Table 6.5 of the Licensing Report provides a summary of the maximum instantaneous fuel-to-rack impact loads for various rack loading cases analyzed. From Table 6.5, the maximum instantaneous impact load is 339 lbs/cell. For the limiting case (Rack C, SSE, μ = 0.8, full load), the maximum instantaneous impact loads by elevation location and direction are as follows:

Maximum Instantaneous Impact Loads (lbs)

	Direction[1]	
Location	X	Y
Top	174	253
3/4 Elev.	114	160
1/2 Elev.	110	160
1/4 Elev.	95	339
Bottom	53	137

(1) X = short rack direction, Y = long rack direction

Analyses performed by General Electric (GE) in support of ensuring fuel system compliance with the requirements of the Standard Review Plan Section 4.2, Appendix A "Fuel System Design", show maximum expected loads on the spacers that are approximately equivalent to the 339 lb peak fuel-to-rack impact load.

GE's fuel system design analyses are proprietary. However, GE tests have shown that the spacer has a design margin greater than 100% over maximum expected seismic reaction loads. In addition, GE analyses show design margins of 50% for the fuel rod over the maximum expected seismic reaction loads.

The Authority concludes that the stresses in the fuel rods will not exceed design margins as a result of fuel-to-rack impacting during a seismic event.

NRC Question 4

P. 6-31. In page 6-31, a discussion regarding difference in responses between a simple and multi-rack analysis was presented. The discussion refers to movements of the support foot. Please provide comparisons in terms of maximum displacements and stresses of fuel rods, as well as at key corresponding nodes between the two analyses.

NYPA Response:

The rack-to-fuel impact loads predicted by the three dimensional (3-D) single rack model are considered to be more accurate than those predicted by the two dimensional (2-D) multi-rack model. This is because the 3-D model determines the maximum instantaneous impact load at 5 elevations which cannot be done with the 2-D model.

The 2-D multi-rack analysis predicts the kinematic displacements of several racks in combination under the same dynamic loading. The primary purpose of the 2-D multi-rack analysis is to confirm that no rack-to-rack or rack-to-wall impacts occur under the postulated loading conditions.

Tables 6.5 and 6.6 of the Licensing Report summarize the various single-rack computer runs. The run that most nearly represents the multi-rack 2-D case is Run B10 for Rack B1. The following is a summary of the loading conditions and results for Rack B1 from the single-rack (Tables 6.5 and 6.6) and multi-rack (Table 6.10) evaluations:

	3-D Single Rack	2-D Multi-Rack
Loading Conditions:		
	Input	
Rack No:	B1	B1
μ (coef. of fric.)*	0.8	0.5
Load	Full	Full
Type of Fuel	Regular	Regular
Earthquake	SSE	SSE
	Output	
Displacement at Rack Top (in.)	.0939	.08129
Rack-to-Fuel Impact Load (lb.):	124	94.7
Rack-to-Rack Impact Load (lb.):	0	0
Rack-to-Wall Impact Load (lb.):	0	0

* Please refer to Section 6.0 of the Licensing report for this variation in coefficient of friction.

The above comparison indicates that the 3-D single rack and 2-D multi-rack models provide consistent and comparable results regarding displacements and impact loads.

Please note that rack-to-fuel impact loads in both cases, i.e., 124 lbs for single rack and 94.7 lbs for multi-rack, are each less than 339 lbs. The Authority's response to Question 3 showed that 339 lbs is acceptable for fuel rod stresses.

NRC Question 5

P. 9-1. Provide key stresses (or strength) and applicable margins that correspond to each load combination. Provide an estimate of the potential increase in stress (decrease in margin) if the current load is calculated using non-linear limit strength analysis. Also provide approximate increase in loads from current to proposed maximum loads for the pool structure.

Supplement to NRC Question 5

During a phone conversation, the NRC requested information about the spent fuel pool dimensions.

NYPA Response:

Applicable Load Combination

An evaluation of the spent fuel pool structure was performed using the weight of the consolidated racks with their contained fuel assemblies and control rods. The load combination that produced the maximum stresses is:

$$U = 1.4D + 1.4F + 1.7L + 1.9E_o$$

where:

U	=	Load Combination
D	=	Dead Load
F	=	Hydrostatic Pressure
L	=	Fully Loaded Racks, Note that racks were considered live load for conservatism.
Eo	=	OBE Earthquake

Key Stresses and Margins for Shear Capacity

The evaluation for shear capacity was performed using elastic (linear) analysis. The total factored load is assumed to be spread out on the pool floor as a uniform applied load. The critical section for shear is taken at a distance "d" in accordance with Section 9.2 of ACI 349-85, modified per section 3.8.3 of the USNRC Standard Review Plan, Revision 1, July 1981. This distance "d" is 57.5" from the extreme compression fiber to the centriod of longitudinal reinforcing steel. Figure 2, shows that most of the currently proposed additional racks will be within the distance "d" from the wall. This will allow the entire load to be directed to the wall and therefore, will have only a minor effect upon shear stresses.

Key Stresses and Margins for Bending Moment Capacity

The critical location for the slab bending moment under the existing high density racks is at the west wall. However, the new racks are to be installed along the east (opposite) wall. Due to this location, the new racks will have no significant effect upon negative bending moments

HARSTEAD ENGINEERING ASSOCIATES • INC.
69 KINDERKAMACK ROAD PARK RIDGE, N.J. 07656

PROJ NO 8903
C- 2 - - 1
SUBJ SUBDIV. SHEET

PROJECT SPENT FUEL STORAGE POOL
CLIENT NYPA
SUBJECT HOLTEC RACKS

PREP BY GH DATE 3/7/91
CHCKD BY AJ DATE 3/13/91

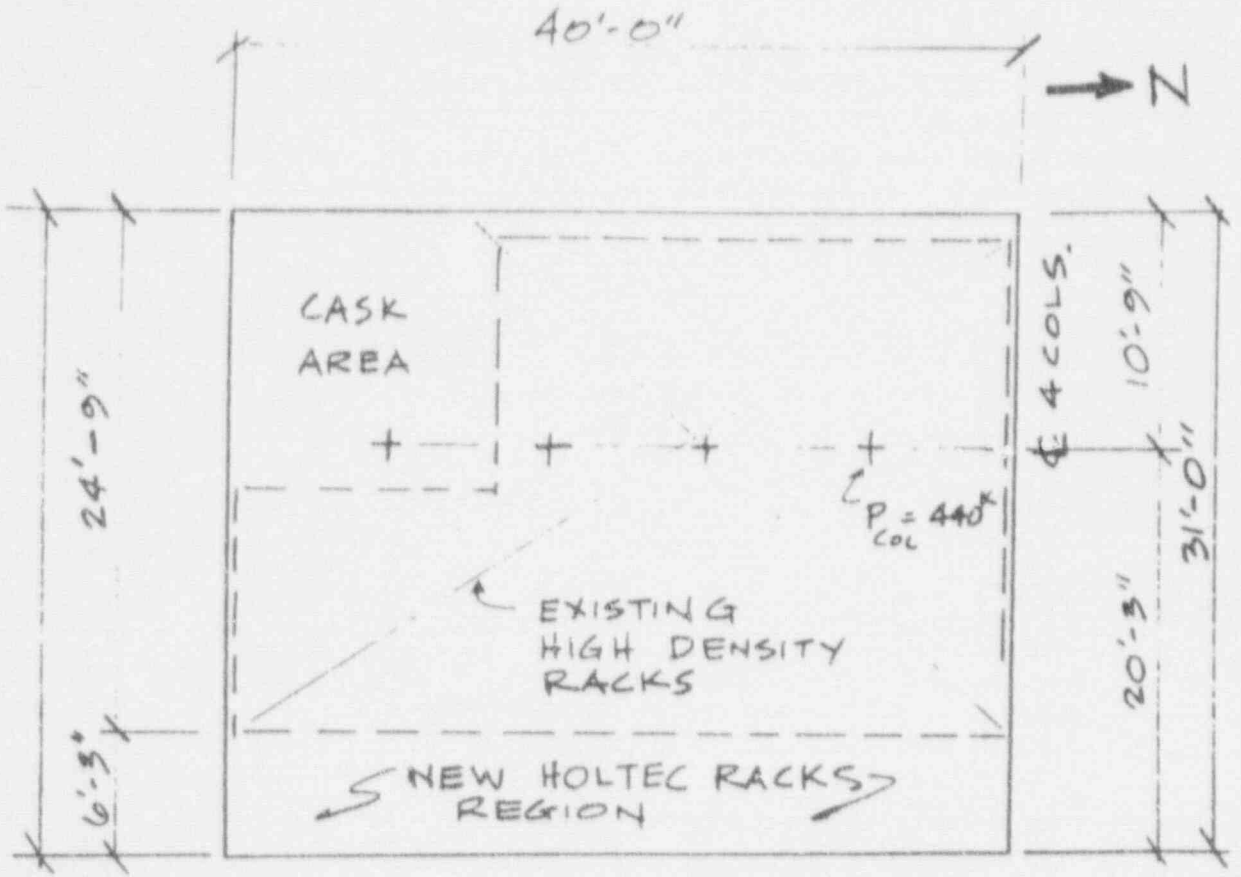

PLAN - SPENT FUEL STORAGE POOL

Figure 2

along the west, north and south walls and only marginal effects, in fact, along the east wall itself.

For the existing racks and the new racks, the slab remains elastic. The step-by-step part of the analysis used to simulate nonlinear response was only needed to determine ultimate capacity.

Potential decrease in margin (increase in stress)

Based upon evaluations of the present high density fuel storage racks, as well as the additional new racks, the margins calculated for the load combination are compared as follows:

	Margin as Percentage of Capacity	
	Current	Proposed
Shear	19	13
Bending Moment	37	34

The comparison above shows that the addition of the new racks along the east edge of the pool does not significantly reduce margins. The new racks are close to the edge and therefore will have little effect upon bending moments. Similarly, most of the load of the new racks will have no effect upon shear at the critical section for shear.

Spent Fuel Pool Dimensions

The dimensions of the pool slab are 31 ′ - 0" wide x 40 ′ - 0" long x 5 ′ - 0" thick. The slab is supported by four additional steel columns located 10 ′ - 9" from the west wall. These columns are 24" in diameter with Belleville springs at the base. Each column was designed to provide a constant upward force of approximately 440 kips on the slab. These columns were added when the original racks were replaced with high density racks. Figure 2 provides a schematic of the spent fuel storage pool.

Proposed maximum loads for the pool structure

In response to this part of the question, attached is Table 9.1 revision 1. This table shows that the percentage increase in loading on the pool structure from "current" to "actual" is only 9%, whereas the structure remains elastic for an increase of up to 52%.

Table 9.1 Revision # 1

Comparision of Current, Actual and Assumed Loads
'or Analysis on Pool Structure

	Current*	Proposed	Assumed
No. of storage cells	2244	2797	2854
Weight per cell	655	730**	1324***
Water height	37.75'	37.75'	37.75'
Total Load (lbs.)	4,390,764	4,794,454	6,699,640

* This column is added in response to Question 5.

** 730 lbs/cell is for additional 553 locations only; existing 2244 locations remain at 655 lbs/cell.

*** Weight corresponding to consolidated fuel was assumed in the slab analysis.

NRC Question 6 — P. 9-1. Provide ANSYS code verification documents regarding non-linear limit strength analysis that is used for the rerack licensing application. The verification should be based on physical, prototypical test data or a closed form solution, as applicable.

NYPA Response: — Nonlinear portions of the ANSYS computer code were not used. Instead, the ANSYS revision 4.1 computer code was used for this analysis. This methodology is a step-by-step elastic (linear) analysis. The verification of ANSYS revision 4.1 computer code is non-proprietary and is available in the public domain. The Authority believes that the NRC has a copy of this verification in house.

NRC Question 7 — Page 6-3. In the second of the three step analysis, the solution is said to be attained using the "Component element time integration scheme." However, in page 6-15, it is stated that numerical solution is obtained using a central difference scheme. This potential confusion should be clarified by specifically discussing the basic formulations of each of the two integration schemes. If the component element time integration scheme is different from the central different scheme, then, one needs to state which one is actually used for the solution of the governing differential equation of motion. Then as in question 2, one should provide verification of the code including error estimates.

NYPA Response: — The component element time integration scheme is different from the central difference scheme. The Authority used the central difference scheme for the solution of the governing differential equation of motion. The integration algorithm used in NYPA's Reference 1 and in the Holtec DYNARACK computer code is the classical central difference method.

The verification of the Holtec DYNARACK computer code, including error estimates, is proprietary and has been reviewed by the NRC for other licensing applications.

NYPA's References:

1. "The Component Element Method in Dynamics with Application to Earthquake and Vehicle Engineering," S. Levy and J.D.D Wilkinson, McGraw Hill 1976.

ATTACHMENT II TO JPN-91-037

HOLTEC REPORT HI-91614
DYNARACK SIMULATIONS TO DEMONSTRATE THE ABILITY TO PREDICT CLASSICAL NONLINEAR PHENOMENA

(JPTS-89-035)

New York Power Authority

JAMES A. FITZPATRICK NUCLEAR POWER PLANT
Docket No. 50-333

HOLTEC
INTERNATIONAL

DYNARACK SIMULATIONS TO DEMONSTRATE THE ABILITY TO PREDICT CLASSICAL NONLINEAR PHENOMENA

by

A.I. Soler

Holtec Report HI-91614
Holtec Project 10290
Report Category: I

SUMMARY OF REVISIONS

Holtec Report HI-91614

Revision 0 contains the following pages:

Title Page	1
Review & Certification Log	1
Summary of Revisions Page	1
Executive Summary	1
Section 1	1
Section 2	20
Appendix A	2
Appendix B	9
Appendix C	4

EXECUTIVE SUMMARY

This report contains results of additional verification studies on Holtec computer code DYNARACK performed to demonstrate DYNARACK's capability to simulate certain unusual and arcane characteristics exhibited by some nonlinear systems. This report is a sequel to the original DYNARACK Q.A. validation report, and it was undertaken to establish DYNARACK's ability to simulate the so-called "jump" and subharmonic response phenomena associated with certain nonlinear systems. Towards this end, sample dynamic problems were selected from the literature and were analyzed on DYNARACK. These problems demonstrate DYNARACK's ability to capture both standard and special characterizations of nonlinear systems.

1.0 INTRODUCTION

This report provides verification that the Holtec dynamic simulation code DYNARACK* is able to predict certain classical nonlinear phenomena that have been found to exist in certain dynamic systems. In particular, we address here the simulation of Coulomb friction by piecewise linear springs, the development of subharmonic resonance, the establishment of limit cycles, and the prediction of nonlinear "jumps" in the solution depending on the direction of loading.

Four problems are addressed in this report which show that the computer code is capable of predicting the classical phenomena.

---

* Holtec Proprietary Reports: User's Manual (HI-89343, Revision 0); Theory, (HI-87162, Revision 1 and HI-90439, Revision 0), and Verification (HI-87161, Revision 2.)

2.0 NONLINEAR DYNAMIC ANALYSIS PROBLEMS

2.1 Subharmonic Resonance

Consider the generic single degree-of-freedom system shown in Figure 2.1. A mass m is subjected to a driving excitation F(t) or a base excitation y(t). The mass is attached to the surrounding environment by a friction interface, by a gap element $F_g(t)$ with spring rate K_4, and by an elastic spring-damper system that can exhibit at most nonlinear cubic behavior (in Figure 2.1, δ_1 is the extension of the elastic spring). Figure 2.2 shows the behavior of the different elements qualitatively. All of these "spring" elements are coded in DYNARACK; the user need only input the information regarding the degrees-of-freedom that cause the spring extension, and the information concerning spring rate magnitude, etc.

In the initial problem, we assume F(t) = 0, and the coefficient of friction $\mu = 0$ (note that $|P_{LIM}| = \mu F_{LIM}$ where F_{LIM} is an input value or the load from an adjacent compression only stop element that represents the contact). We also assume in this problem that x_0 is large so that the gap element never acts. The nonlinear spring is assumed as ($K_3 = 0$)

$$F_s = -[K_1 \delta_1 + K_2 \delta_1^2]$$

and the input excitation is $\ddot{y}(t) = 10g \sin(2\pi ft)$.

We assume m = .1036 lb.sec.^{2}/in., $C_1 = 0.$, $K_1 = 90$ lb./in., $K_2 = 10$ lb./in.^{2}, f = 9.4 HZ, and g = 386.4 in./sec. For a low amplitude linear excitation, the linear natural frequency is

$$f_o = \frac{1}{2\pi}\left(\frac{K_1}{m}\right)^{\frac{1}{2}} = 4.69 \text{ HZ}$$

If we integrate $\ddot{y}(t)$, and require that there be no rigid body base motion, then

$$\dot{y}(0) = \frac{10g}{2\pi f} = -65.4228 \text{ in./sec.} \qquad y(0) = 0$$

To ensure that the spring is initially unstretched, we assume the same initial conditions on the mass m.

Figure 2.3 shows the acceleration of the mass versus time. The subharmonic resonance is clearly visible in that there is a strong response at 4.7 HZ (half the frequency of the imposed driving excitation). Appendix A contains numerical results for the same problem done in Reference 6.6.

2.2 Sliding Friction and Dead Bands

Consider Figure 2.1 for the case $x_o \to \infty$, $F_S = 0$, $C_1 = 0$, $F(t) = B \sin rt$. That is, we consider a mass resting on a frictional surface which generates a frictional resisting force $\pm R$ and is driven by an external sinusoidal force. Tou and Schutheiss* have given solutions for this situation. The interesting features of the motion are that if $R/B < .536$, the motion is roughly sinusoidal, but has discontinuities in acceleration. If $R/B > .536$, then the motion is sporadic, there being so-called dead bands

---

* "Static and Sliding Friction in Feedback Systems, J. Tou and P.M. Schultheiss, Jour. Appl. Physics, Vol. 24, 9, September 1953, pp 1210-1217.

within which no motion occurs. When $R/\beta > 1$, no motion is possible except for an initial transient. Appendix B contains a copy of the reference. Here, we use DYNARACK to model the phenomena. The governing equation is

$$m \frac{d^2 x}{dt^2} = \beta \sin wt \pm R$$

We simulate the event for $m = \beta = 1$, and $R/\beta = \lambda = .3, .7$, and 1.01. The friction spring constant (Figure 2.2) is set at $K_f = 1 \times 10^7$ lb./in. to simulate an "infinite" slope. Figures 2.4 - 2.6 show the results for the three values of λ. It is clearly evident that DYNARACK is capable of reproducing the expected phenomena. In Figure 2.6, the small non-zero velocity components subsequent to the initial transient are due to the presence of the finite K_f.

2.3 Jump Phenomena

Consider the differential equation

$$m \ddot{x} + b \dot{x} + cx + dx^3 = E \sin \upsilon t$$

We let $x_1 = (d/c)^{1/4} x$; $t_1 = (c/m)^{1/4} t$

Then the differential equation becomes

$$\frac{d^2 x_1}{dt_1^2} + \delta \frac{dx_1}{dt_1} + x_1 + x_1^3 = E_1 \sin \upsilon_1 t$$

where x_1, t_1, E_1, υ_1, δ are dimensionless and

$$\delta = b/c \ (c/m)^{1/4} \quad E_1 = E/C \ (d/c)^{1/4} \quad \upsilon_1 = \upsilon(m/c)^{1/4}$$

An approximate first order asymptotic solution is obtained analytically by Bogliubov and Mitropolsky.*

For an assumed oscillatory solution

$$x_1 = a \cos (\nu_1 t + \theta) \quad a = a(t);\ \theta = \theta(t)$$

the approximate solution for the ν-a resonance curve is

$$w_e^2 = (1 + \frac{3}{8} a^2)^2$$

$$\nu_1 = \{w_e^2(a) \pm \left[\frac{E_1^2}{a^2} - \delta^2 \right|^{1/4} \}^{1/2}$$

For the parameters $\delta = .2$, $E_1 = 1$, the resonance curve can be constructed using using the above approximate analytical solution. A typical result is shown in Appendix C, and tabular results, sufficient to plot the resonance curve, are also given in that appendix.

Note that the solution to the linear non-dimensional equation (neglect the x_1^3 term) predicts the peak amplitude $|x_1|_{max} = 5.0$ at a frequency of .99 rad/sec. It has been shown that a system with a hardening spring has a resonance curve whose central spine is tilted to the right as shown in Figure C-1 in Appendix C. The resonance curve is obtained for a given amplitude of excitation. In practice, the resonance curve shows areas of instability. If the excitation frequency rises, the response follows the resonance curve to a certain point, and then drops abruptly to a smaller amplitude. Similarly, if the excitation frequency is decreased through the resonance region, the response will pass along the

---

* Asymptotic Methods in the Theory of Non Linear Oscillations", by N.N. Bogolinbov and Y.A. Mitropolsky (Translation by Hindustan Publishing Corp., 1961), pp 244-245.

lower curve, to the inflection point, and then abruptly increase to the higher branch. It is found in actual shaker tests that the onset of the instability is sensitive to the sweep rate of the shaker. We attempt here to demonstrate the ability of DYNARACK to predict a jump phenomena. We simulate the resonance curve by doing a time history analysis with $E_1 = 1$, $\delta = .2$, and υ_1 slowly increased from a value less than 1.0 rad/sec. The sweep rate is set low enough to be able to ascertain the maximum response amplitude. Figures 2.7 and 2.8 show the result of the DYNARACK simulation. Figure 2.8 also contains the two branches of the resonance curve plotted from Table C-1 in Appendix C. Both figures show that the simulation code is able to model the jump instability; however, the results show that the onset of instability is very sensitive to the time step size. Figure 2.7 represents a run for 100 seconds with step size .004 sec. while Figure 2.8 shows the curve obtained with a step size of .0001 sec. We see that the amplitude at the onset of instability is relatively insensitive to the step size but the frequency at which the instability occurs is sensitive to the step size. It is apparent that to exactly follow the resonance curve (itself an approximate solution), an extremely fine step size is called for. We did not attempt any modeling of the resonance with a decreasing forcing frequency.

2.4 LIMIT CYCLES

We consider the problem studied in Shaw and Holmes.* to investigate the ability of DYNARACK to predict the existence of stable limit cycles. In the Shaw and Holmes paper, the model

---

* S.W. Shaw and P.J. Holmes, "A Periodically Forced Piecewise Linear Oscillator", Journ. of Sound and Vibration, Vol. 90, 1983, pp 129-155.

described in Figure 2.1 is investigated under the assumptions that friction is absent, the spring F_S is linear, and the excitation is by a harmonic force. The non-dimensionalized equation can be written as

$$\ddot{x} + 2\alpha \dot{x} + H(x) = \beta \cos w t$$

where

$$H(x) = \begin{cases} x & x < x_o \\ \overline{w}^2 x + (1 - \overline{w}^2) x_o & x \geq x_o \end{cases}$$

and $\overline{w}^2 = (K_1 + K_4)/K_1$

Figure 2.9, reproduced from Shaw and Holmes shows different cases of the above equation. The case $x_o = 0$ is considered so the problem is essentially that of a piecewise linear spring having a different spring constant in tension and in compression.

The results from DYNARACK, for the same problems of Figure 2.9, are shown in Figures 2.10 - 2.14. The computer simulation started from a specified initial condition and covered a sufficient number of cycles so that a limit cycle could be established. Figures 2.10 and 2.11 show the match with two problems shown in Figure 2.9. The simulation predicts the one or two stable limit cycles. Figures 2.12 - 2.14 show results of the similar analysis for the third case considered. Figures 2.12 and 2.13 show the effect of different starting conditions. It is clear that only the stable period one orbit is being tracked by the numerical solution. Figure 2.14 is a plot of only the last few hundred time steps and confirms the tendency toward the stable period one orbit. The period three orbit appears unstable which seems to contradict the conclusion in Shaw and Holmes. However, if one reads the text in Figure 2.9, Shaw and Holmes appear to conclude that an <u>unstable</u> period three also exists at the same parameter values. We can only conclude that it is extremely fortuitous if the numerical solution can simulate a stable orbit when an unstable orbit with the same period exists concurrently.

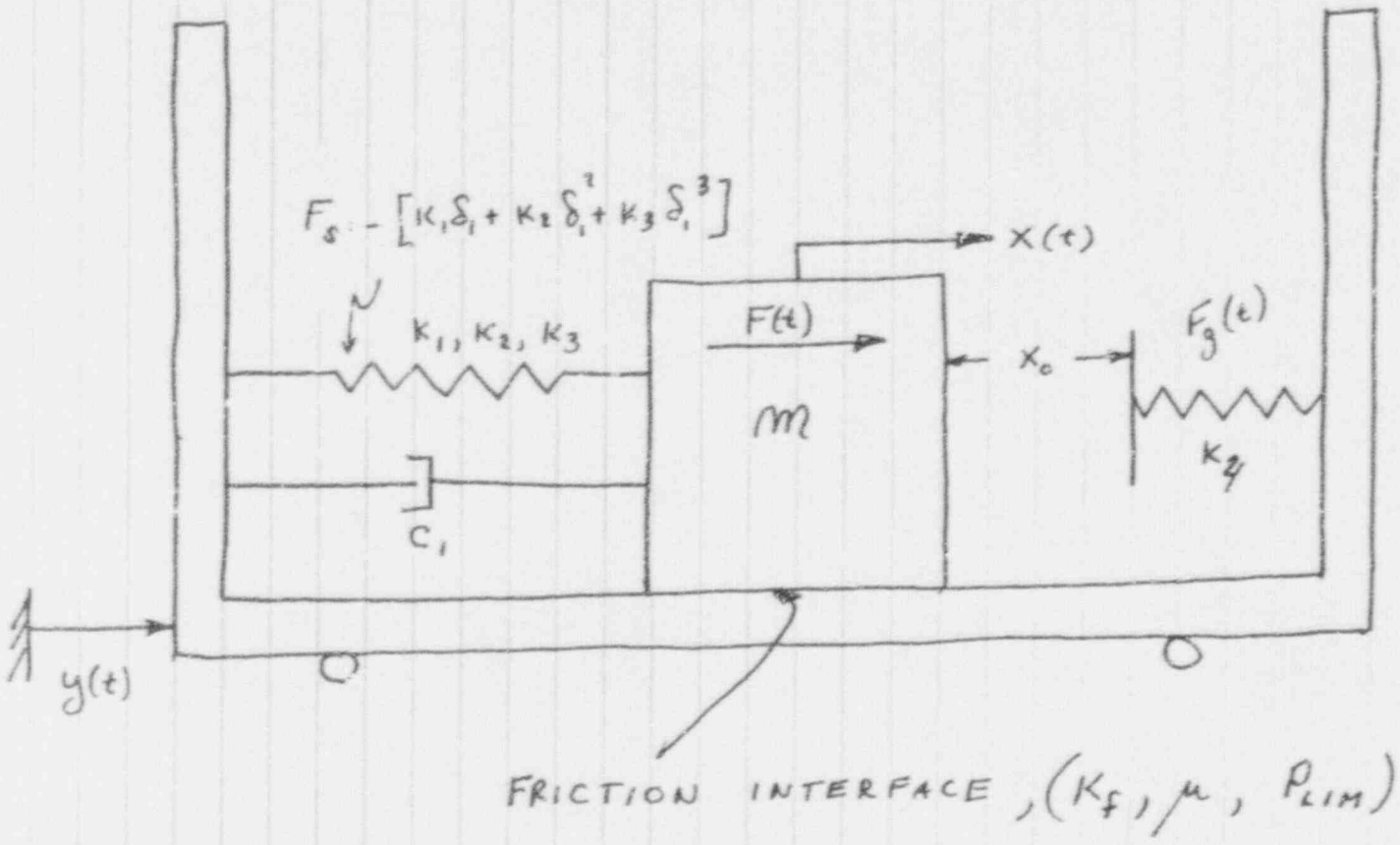

FIGURE 2.1 1-DOF MODEL

FIGURE 2.2 SPRING CHARACTERISTICS

NON LINEAR ELASTIC SPRING

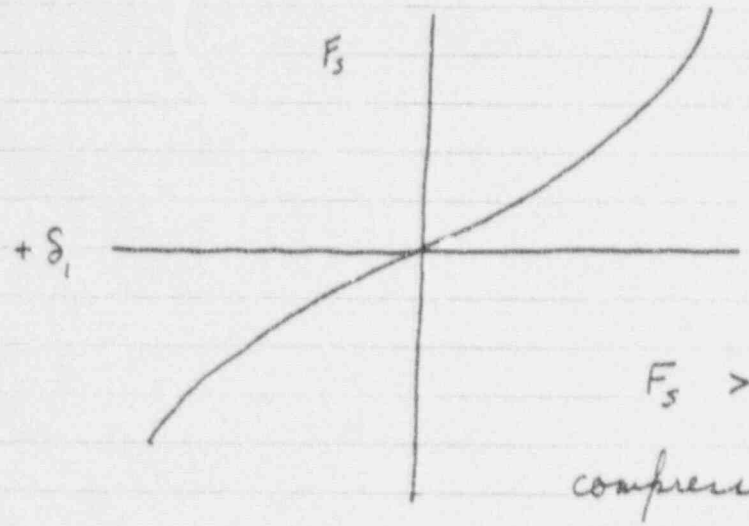

$F_s > 0$ if spring is in compression

COMPRESSION ONLY GAP ELEMENT

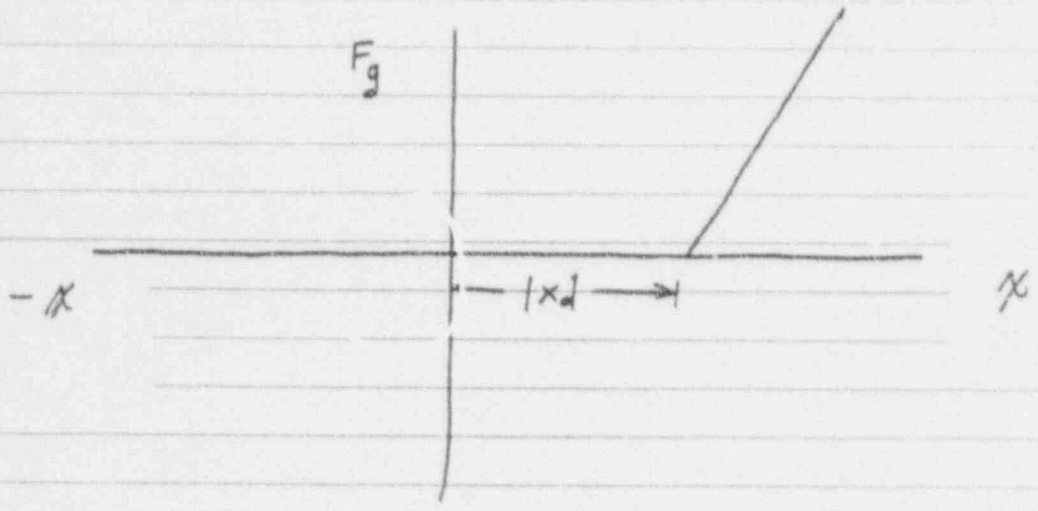

FRICTION INTERFACE ELEMENT

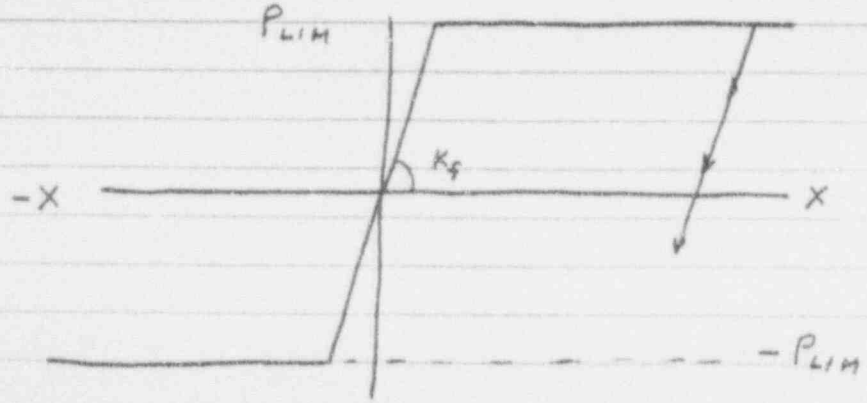

$F_s \dot{X} < 0$

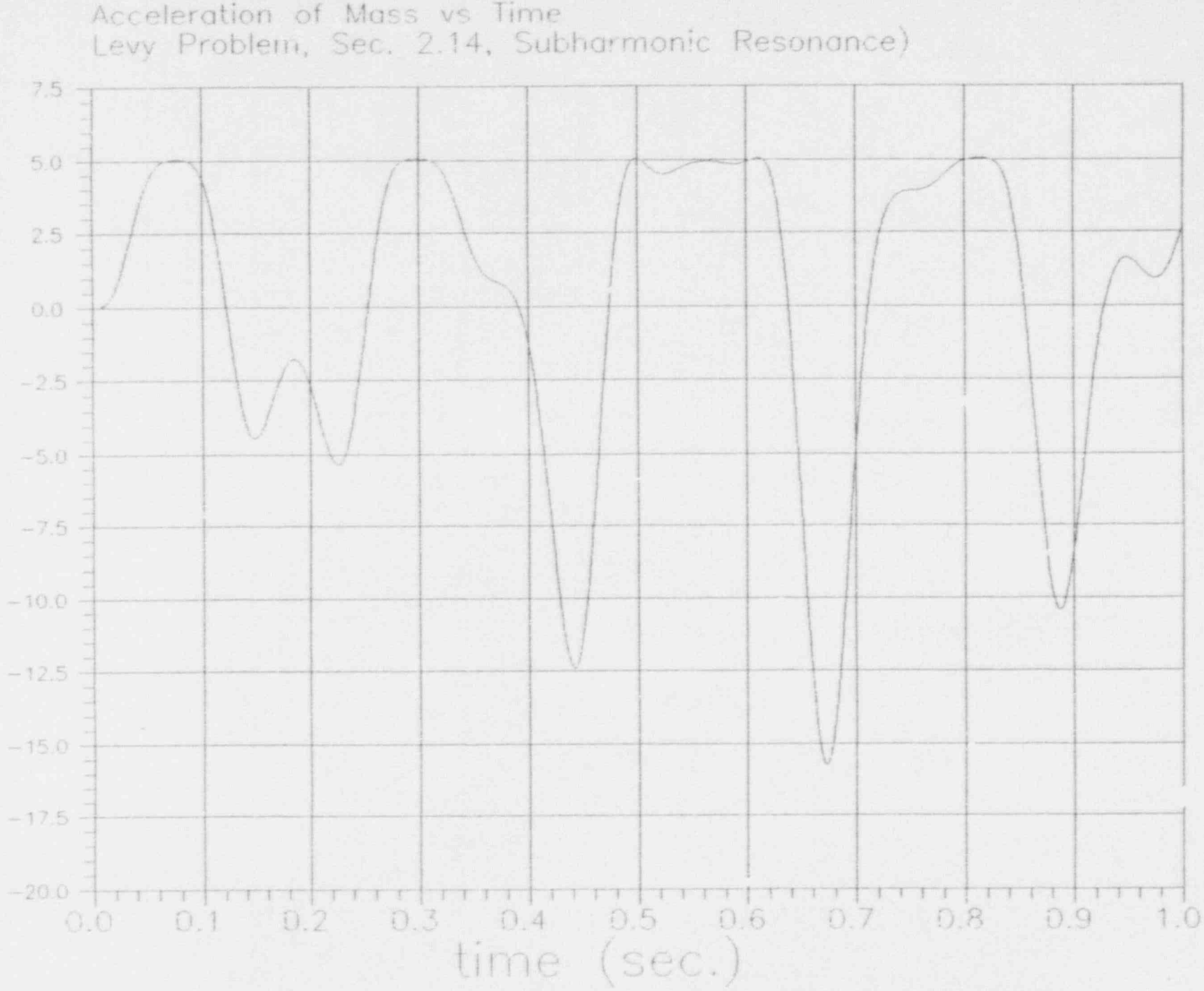
Acceleration of Mass vs Time
Levy Problem, Sec. 2.14, Subharmonic Resonance)
7.5
5.0
2.5
0.0
-2.5
-5.0
-7.5
-10.0
-12.5
-15.0
-17.5
-20.0
acceleration (G's)
0.0
0.1
0.2
0.3
0.4
0.5
0.6
0.7
0.8
0.9
1.0
time (sec.)

FIGURE 2.3

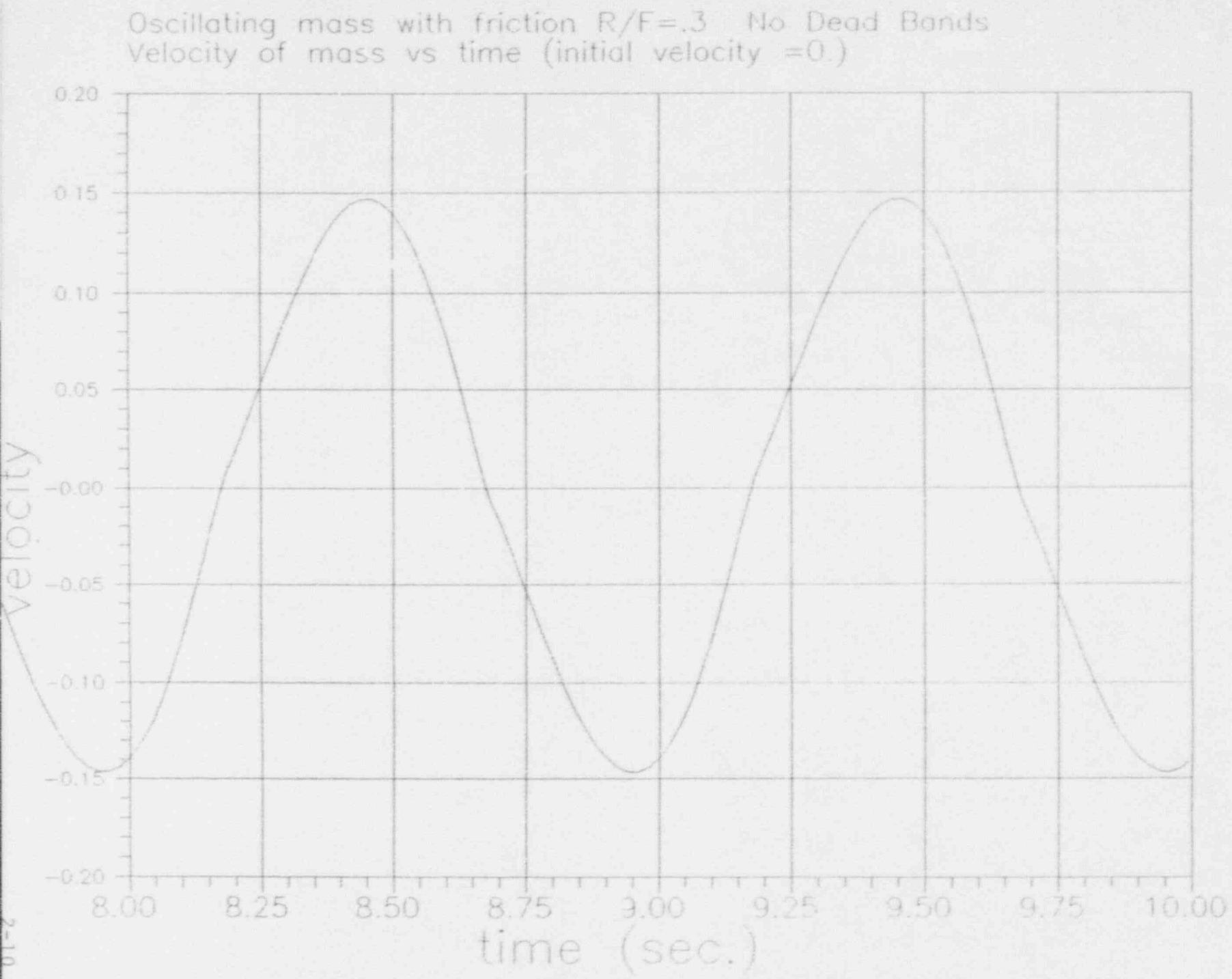
Oscillating mass with friction R/F=.3 No Dead Bands
Velocity of mass vs time (initial velocity =0.)
0.20
0.15
0.10
0.05
-0.00
-0.05
-0.10
-0.15
-0.20
Velocity
8.00
8.25
8.50
8.75
9.00
9.25
9.50
9.75
10.00
time (sec.)

FIGURE 2.4

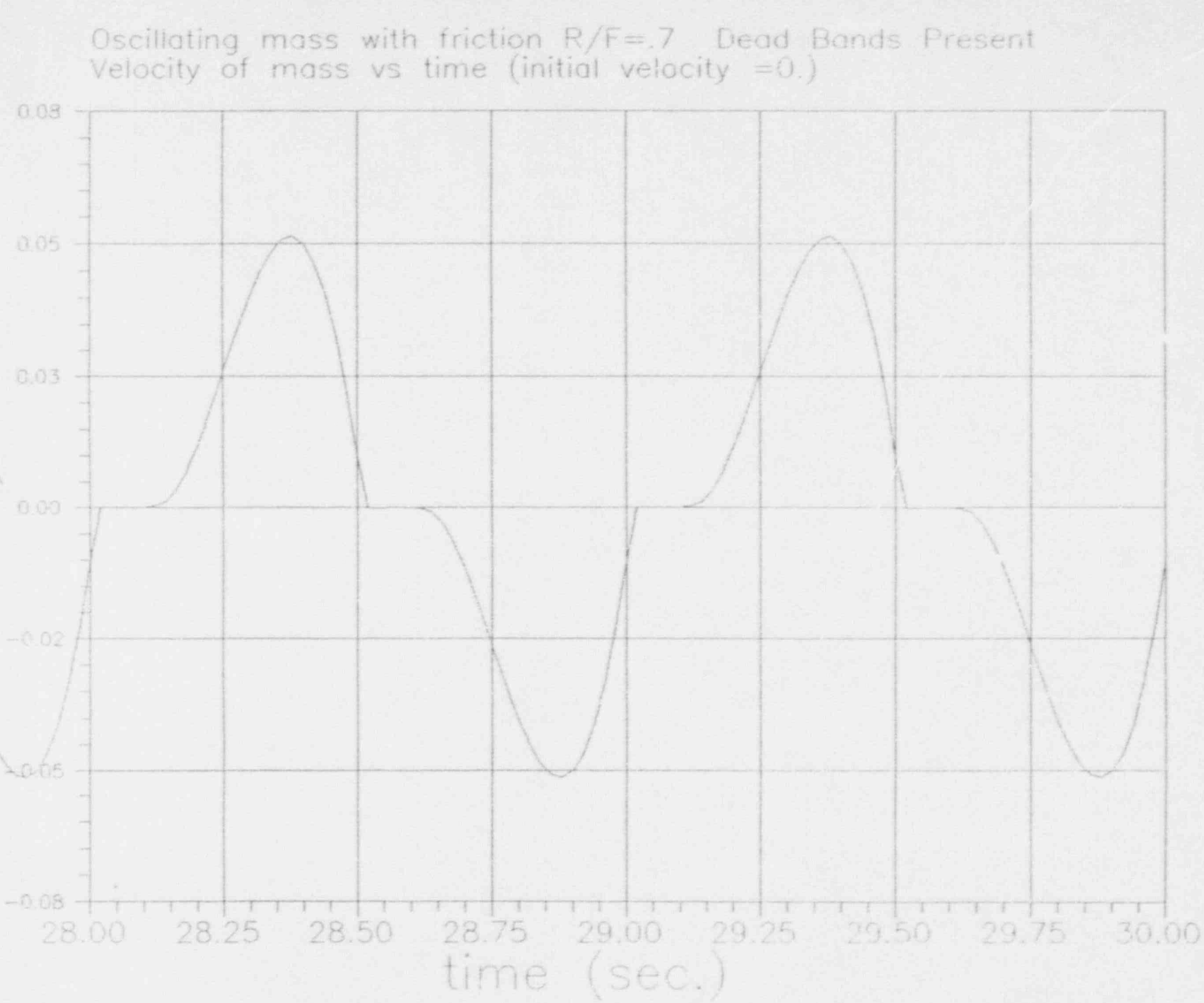
Oscillating mass with friction R/F=.7 Dead Bands Present
Velocity of mass vs time (initial velocity =0.)
0.08
0.05
0.03
0.00
-0.02
-0.05
-0.08
velocity
28.00
28.25
28.50
28.75
29.00
29.25
29.50
29.75
30.00
time (sec.)

FIGURE 2.5

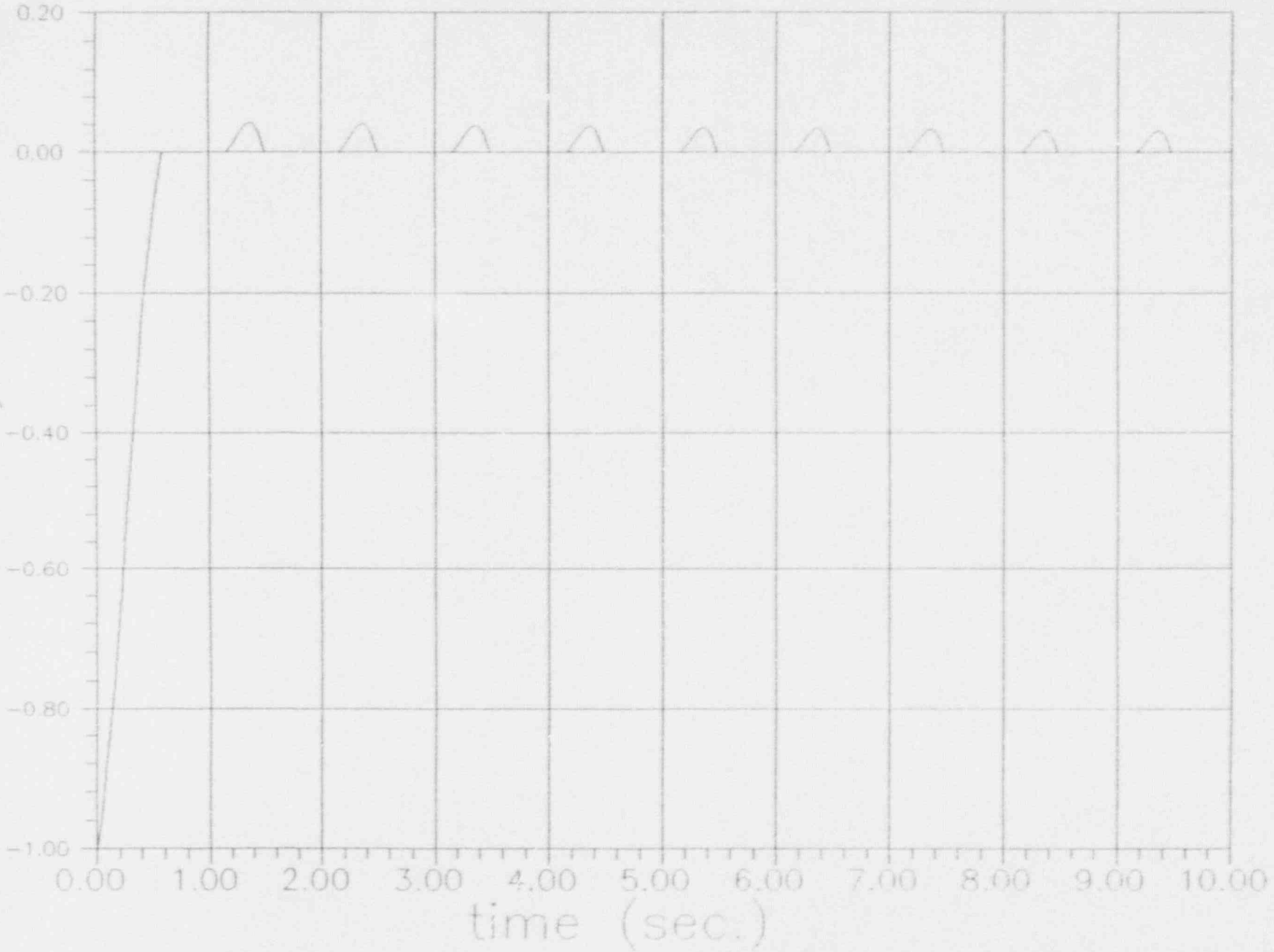
Oscillating mass with friction R/F=1.01 mass eventually stops
Velocity of mass vs time (initial velocity =-1.)
0.20
0.00
-0.20
-0.40
-0.60
-0.80
-1.00
velocity
0.00
1.00
2.00
3.00
4.00
5.00
6.00
7.00
8.00
9.00
10.00
time (sec.)

FIGURE 2.6

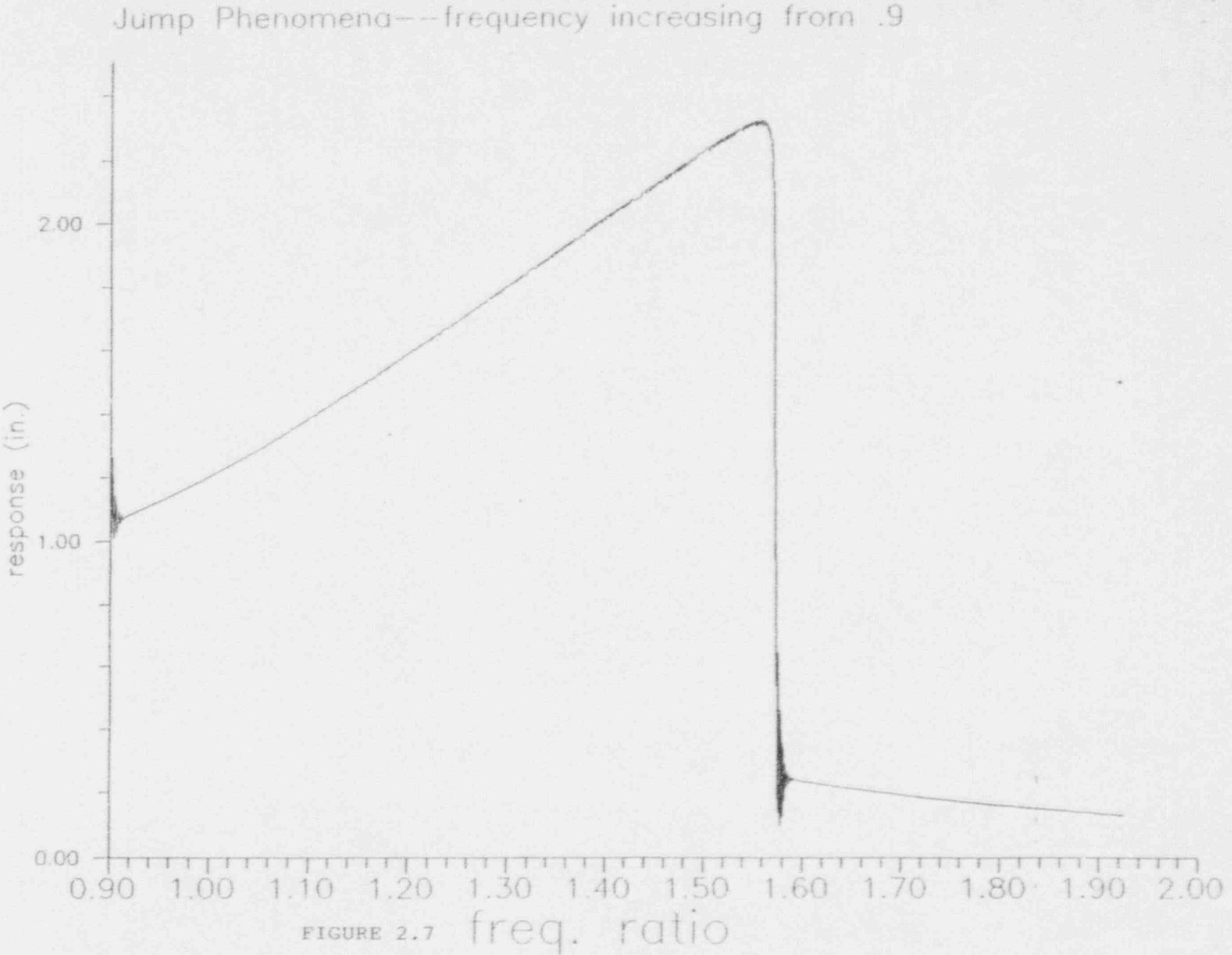
Jump Phenomena--frequency increasing from .9
response (in.)
2.00
1.00
0.00
0.90
1.00
1.10
1.20
1.30
1.40
1.50
1.60
1.70
1.80
1.90
2.00
freq. ratio

FIGURE 2.7

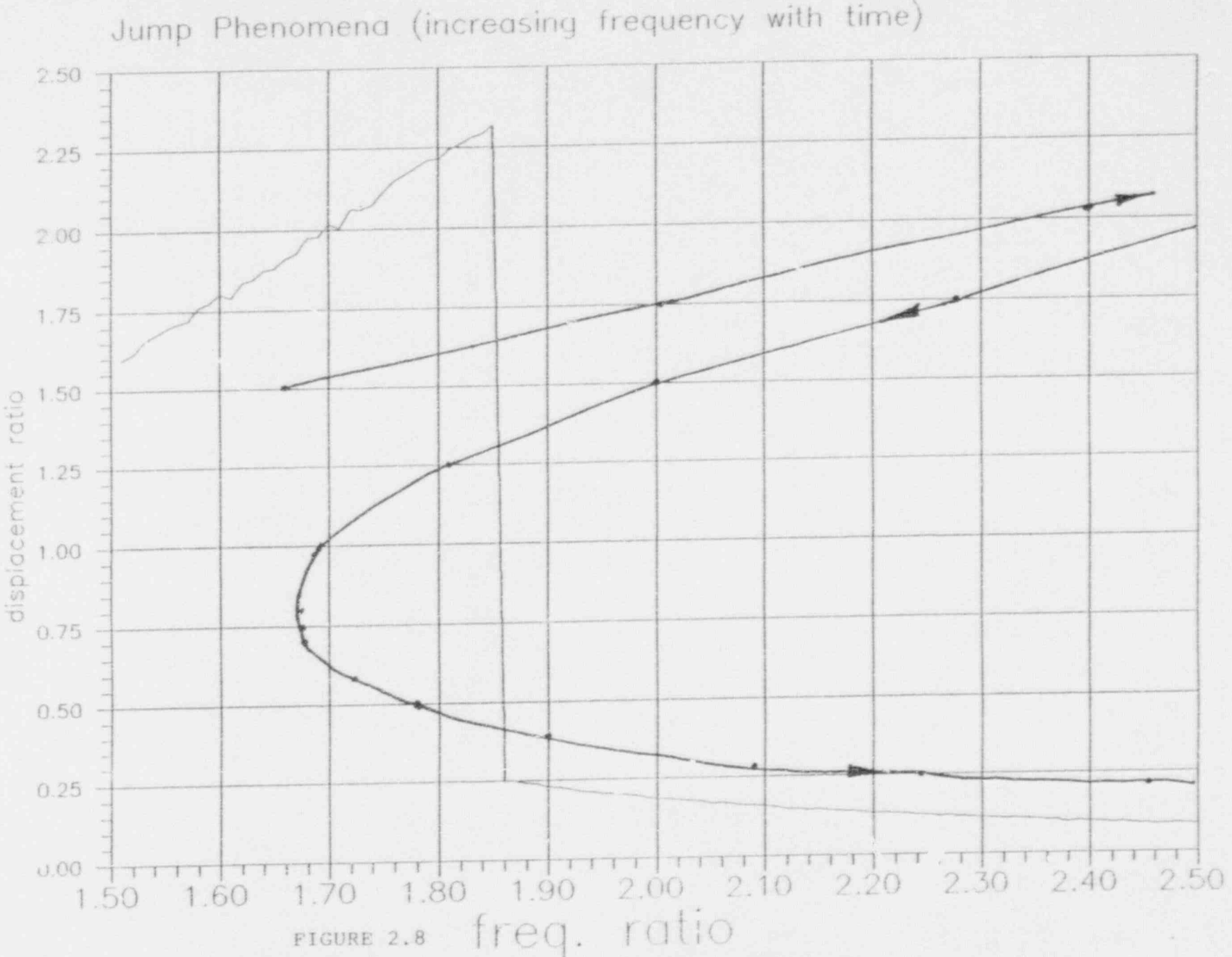
Jump Phenomena (increasing frequency with time)
displacement ratio
2.50
2.25
2.00
1.75
1.50
1.25
1.00
0.75
0.50
0.25
0.00
1.50
1.60
1.70
1.80
1.90
2.00
2.10
2.20
2.30
2.40
2.50
freq. ratio

FIGURE 2.8

FIG. 2.9 (REPRODUCED TEXT)

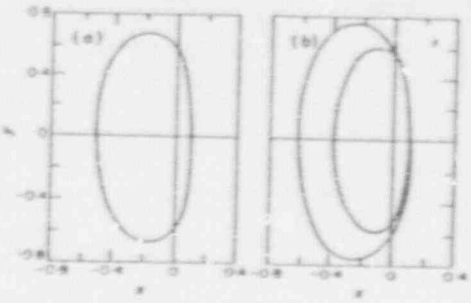

Figure 8. (a) Stable period one orbit at $\omega = 2{\cdot}40$, $\alpha = 0{\cdot}125$, $x_0 = 0$, $\beta = 1$, and $\bar{\omega} = 4$, from digital simulation; (b) stable period two orbit at $\omega = 7{\cdot}42$, $\alpha = 0{\cdot}125$, $\beta = 1$, $x_0 = 0$, and $\bar{\omega} = 4$, from digital simulation. Both in projected phase plane $(x, \dot{x})$.

By using digital simulations, other subharmonic orbits are also found to exist. Figures 9(a) and (b) show the coexistence of single impact stable period one and stable period three orbits for $x_0 = 0$, $\alpha = 0{\cdot}026$, $\bar{\omega} = \sqrt{2}$ and $\omega = 3{\cdot}5$. We conjecture that the period three orbit appeared in a saddle-node bifurcation [21] and that an unstable period three orbit also exists at these parameter values. Analysis of this bifurcation is much more difficult since no reasonable assumption regarding the times of flight can be made and higher iterates of the mapping (multiple impacts) appear to be involved.

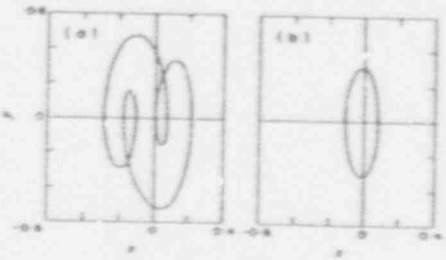

Figure [illegible] stable period three and stable period one at $\bar{\omega} = \sqrt{2}$, $\alpha = 0{\cdot}026$, $\beta = 1$, $x_0 = 0$ and $\omega = 3{\cdot}5$. (a) [illegible] period 1. Both in projected phase plane $(x, \dot{x})$.

4.3. THE IMPACT LIMIT, ANALYSIS

In the impact limit an important simplification occurs, since the time of flight during the impact is taken to be zero. This allows more analysis to be done on periodic orbits. We also rescale: $x \to \beta x$, and take unit forcing amplitude.

The return map for the impact oscillator is very similar to the one for the general system. From points 0 to 1 in Figure 4 one uses the impact limit, i.e.,

$$t_1 = t_0, \quad \text{and} \quad y_1 = -ry_0. \tag{49}$$

From points 1 to 2 one uses the same mapping as described in the general case. Thus the mapping $\mathbf{P}$ still cannot be written down explicitly. As before, however, one can compute $\mathbf{DP}$ analytically. Moreover, in this limiting case one can compute periodic points corresponding to single impact, period n orbits directly. Such orbits correspond to those motions which strike the wall (the very stiff spring k_2) and then remain in $x < x_0$ for

exactly $2\pi n/\omega$ in time and then strike the wall again with the same velocity as the previous impact. The conditions for the existence of such an orbit are

$$t_2 - t_0 = 2\pi n/\omega, \qquad y_2 = y_0 = -y_1/r, \quad \text{with} \quad y_0 > 0. \tag{50, 51}$$

These two conditions allow one to compute the period n point $(\bar{x}, \bar{y})$. First one writes equation (7), using equations (5), (50), and (51), to obtain

$$0 = -x_0\Gamma_- + Ay_1 + s_1(\delta\Gamma_- + A\gamma\omega) + c_1(\gamma\Gamma_- - A\delta\omega), \tag{52}$$

where we have dropped the minus subscripts on γ, δ, and Ω and where $\Gamma_\pm = 1 - Ec \pm \gamma A$, $A = Es/\Omega$, $E = e^{-2\pi n\zeta/\omega}$, $s = \sin(2\pi n\Omega/\omega)$, and $c = \cos(2\pi n\Omega/\omega)$. Next one writes equation (51) using equation (50) and the time derivative of equation (5) to obtain

$$0 = y_1(-1 - r + r\Gamma_+) + Arx_0 + s_1 r(\gamma\omega\Gamma_+ - A\delta) - c_1 r(\delta\omega\Gamma_+ + A\gamma). \tag{53}$$

Since y_1 appears in a linear manner in both equations (52) and (53), it may be eliminated to obtain a single equation involving only t_1 as an unknown (in the terms $c_1 = \cos(\omega t_1)$ and $s_1 = \sin(\omega t_1)$):

$$\begin{aligned} 0 = (x_0/A)[rA^2 - \Gamma_-\phi] + s_1[r\gamma\omega\Gamma_+ - A\delta r + (\phi/A)(\delta\Gamma_- + A\gamma\omega)] \\ + c_1[-r\delta\omega\Gamma_+ - A\gamma r + (\phi/A)(\gamma\Gamma_- - A\delta\omega)], \end{aligned} \tag{54}$$

where $\phi = 1 + r - r\Gamma_+$. Straightforward association of terms allows this equation to be written as

$$0 = X + s_1 Y + c_1 Z, \tag{55}$$

which has a solution

$$\bar{t}_1 = (1/\omega)[\arctan(Y/Z) + \arccos(-X/W)], \tag{56}$$

where $W = \sqrt{Y^2 + Z^2}$. This expression gives the time (i.e., forcing phase) at impact on the period n orbit. The velocity just after impact $\bar{y}_1$ is then easily computed by using either equation (52) or equation (53).

It is important to note that a solution obtained as described above only satisfies $x(t_1) = x_0$ and $\dot{x}(t_1) = -r\dot{x}(t_2)$. If the value of $\bar{y}_1 = \dot{x}(t_1)$ is positive, then the solution corresponds to a non-physical, or "penetrating" orbit [13]. The orbits for $\bar{y}_1$ negative must also be checked since nowhere has one been assured that the desired x_0 crossing is the first on the orbit. In fact, the above conditions can be satisfied after several x_0 crossings, for some parameter values. Care must be taken to determine which of these orbits are physically possible.

Knowing the periodic point, one can now compute its stability. As before, one breaks the calculation of $\mathbf{DP}$ into two parts, from point 0 to 1 and from point 1 to point 2. Here

$$\left[\frac{\partial(t_1, y_1)}{\partial(t_0, y_0)}\right] = \begin{bmatrix} 1 & 0 \\ 0 & -r \end{bmatrix}, \quad \text{and} \quad \mathbf{DP} = \left[\frac{\partial(t_2, y_2)}{\partial(t_1, y_1)}\right]\begin{bmatrix} 1 & 0 \\ G & -r \end{bmatrix}, \tag{57, 58}$$

where $[\partial(t_2, y_2)/\partial(t_1, y_1)]$ was derived above in the analysis of the finite stiffness case. From this calculation one finds that $\mathbf{DP}$ has determinant

$$D = (-ry_1/y_2)\,e^{-2\pi\zeta(t_2 - t_0)}, \tag{59}$$

and trace

$$T = [e^{-\pi\zeta(t_2 - t_0)/\Omega y_2}][(N_1 + rN_2)\sin(\Omega(t_2 - t_0)) + \Omega(y_1 - ry_2)\cos(\Omega(t_2 - t_0))]. \tag{60}$$

Evaluating on a period n orbit gives

$$\bar{D} = r^2E^2 \quad \text{and} \quad \bar{T} = (E/\Omega\dot{y}_0)[(1 + r)(\zeta_0 + x_0)s - 2r\dot{y}_0\Omega c], \tag{61, 62}$$

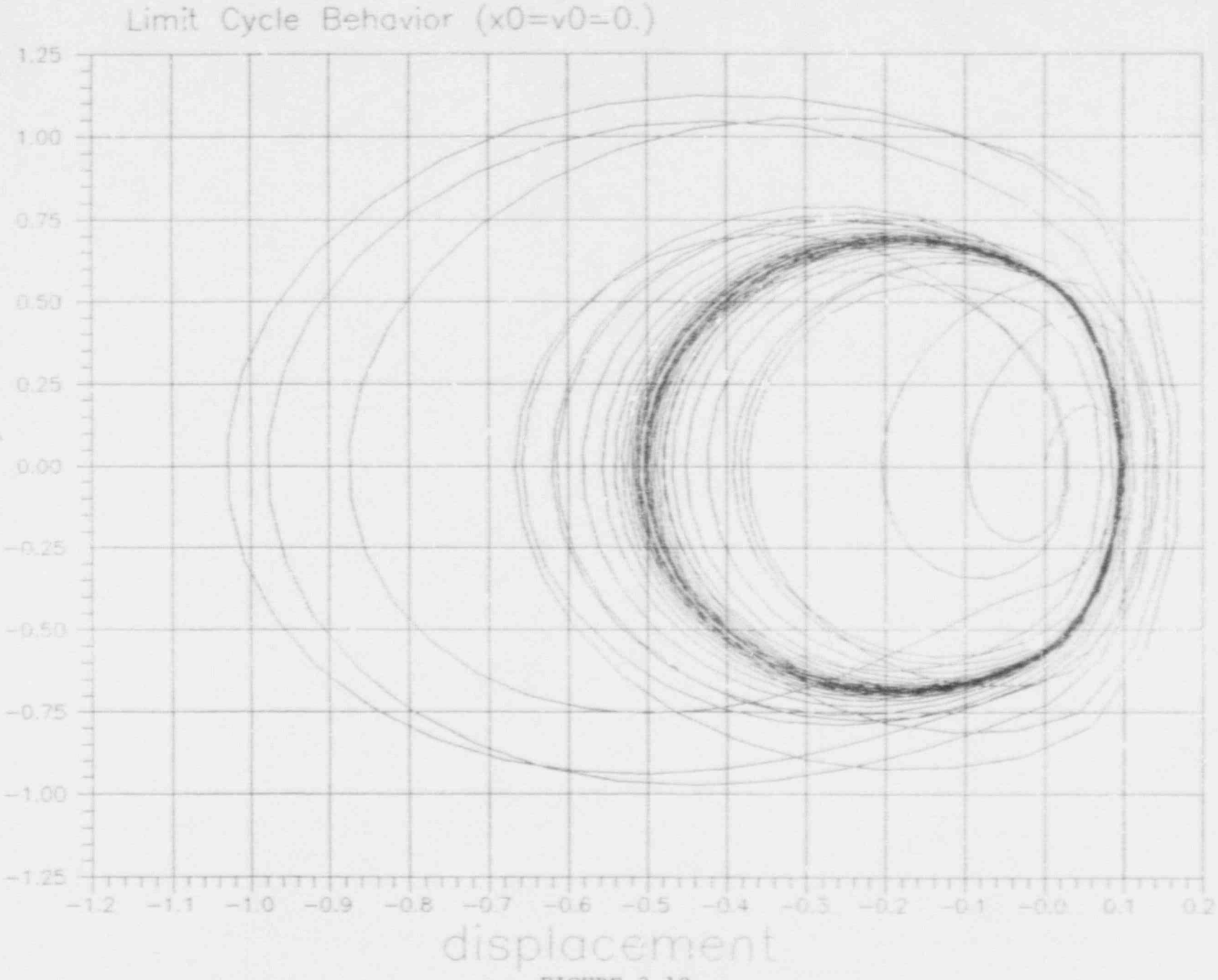
Limit Cycle Behavior (x0=v0=0.)
1.25
1.00
0.75
0.50
0.25
0.00
-0.25
-0.50
-0.75
-1.00
-1.25
velocity
-1.2
-1.1
-1.0
-0.9
-0.8
-0.7
-0.6
-0.5
-0.4
-0.3
-0.2
-0.1
-0.0
0.1
0.2
displacement

FIGURE 2.10

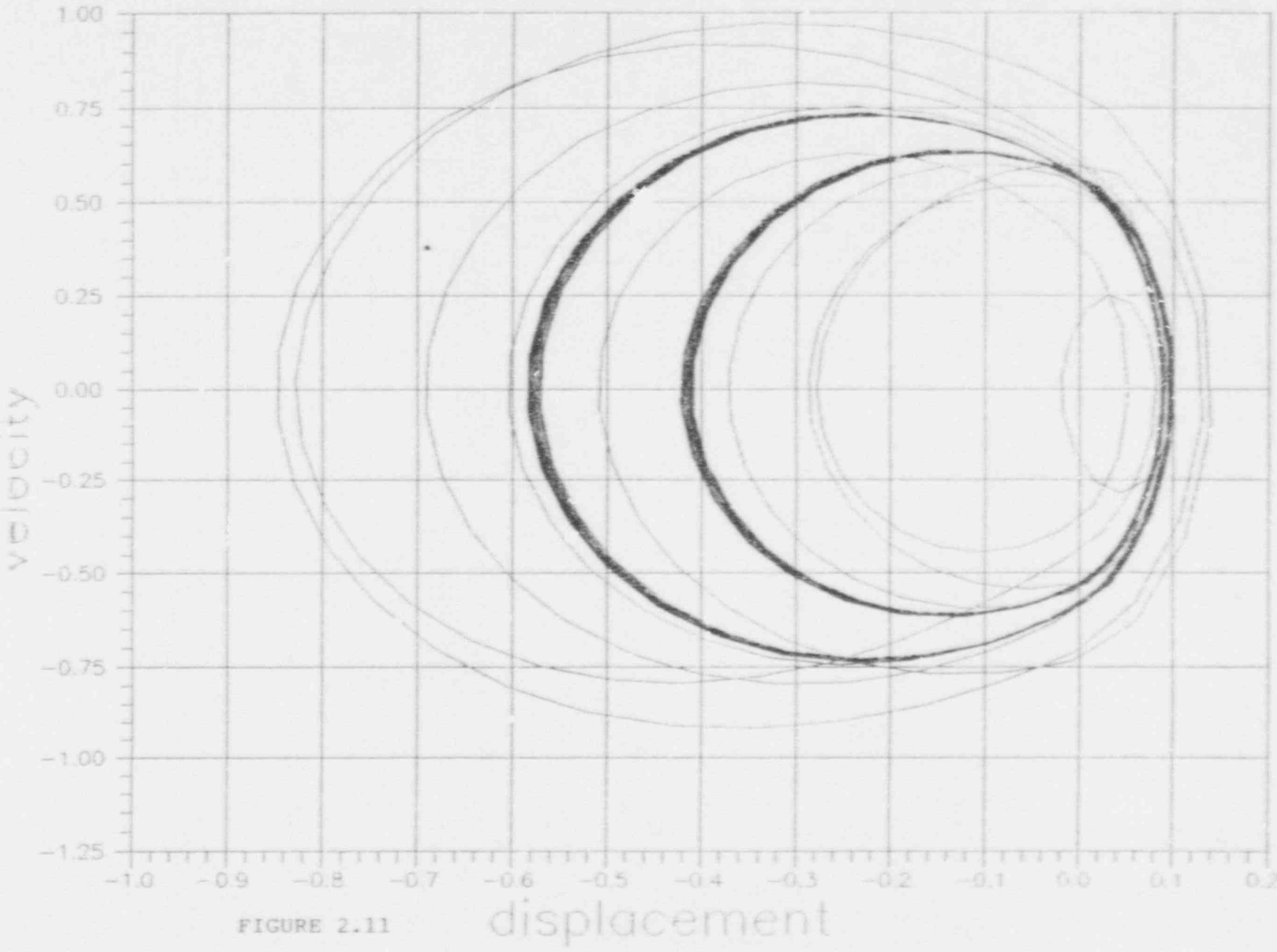
Limit Cycle Behavior (x0=.1,v0=0...Fig. 8b of shaw and Holmes
Shows prediction of two stable limit cycles
1.00
0.75
0.50
0.25
0.00
-0.25
-0.50
-0.75
-1.00
-1.25
velocity
-1.0
-0.9
-0.8
-0.7
-0.6
-0.5
-0.4
-0.3
-0.2
-0.1
0.0
0.1
0.2
displacement

FIGURE 2.11

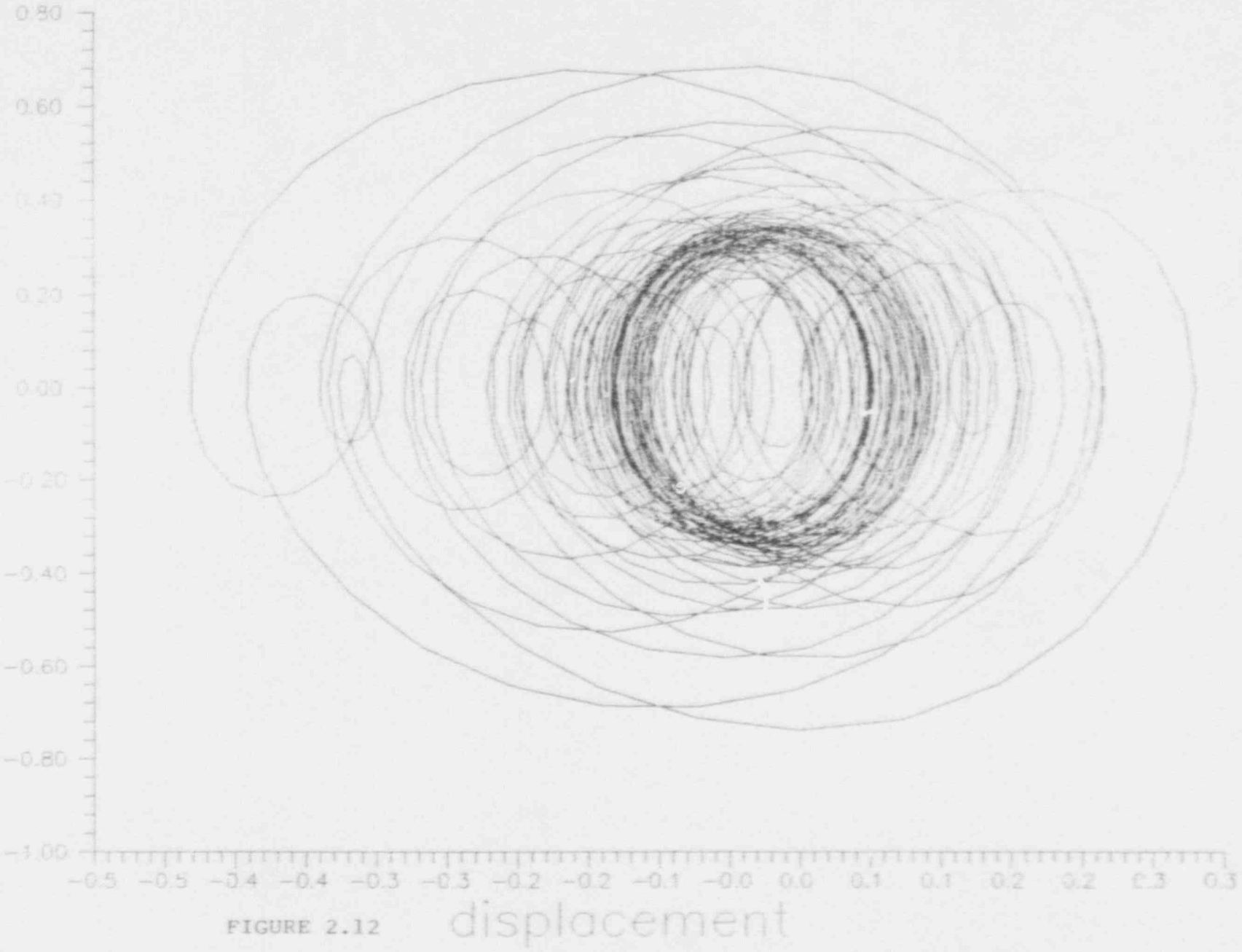
0.80
0.60
0.40
0.20
0.00
-0.20
-0.40
-0.60
-0.80
-1.00
velocity
-0.5 -0.5 -0.4 -0.4 -0.3 -0.3 -0.2 -0.2 -0.1 -0.0 0.0 0.1 0.1 0.2 0.2 0.3 0.3
displacement

FIGURE 2.12

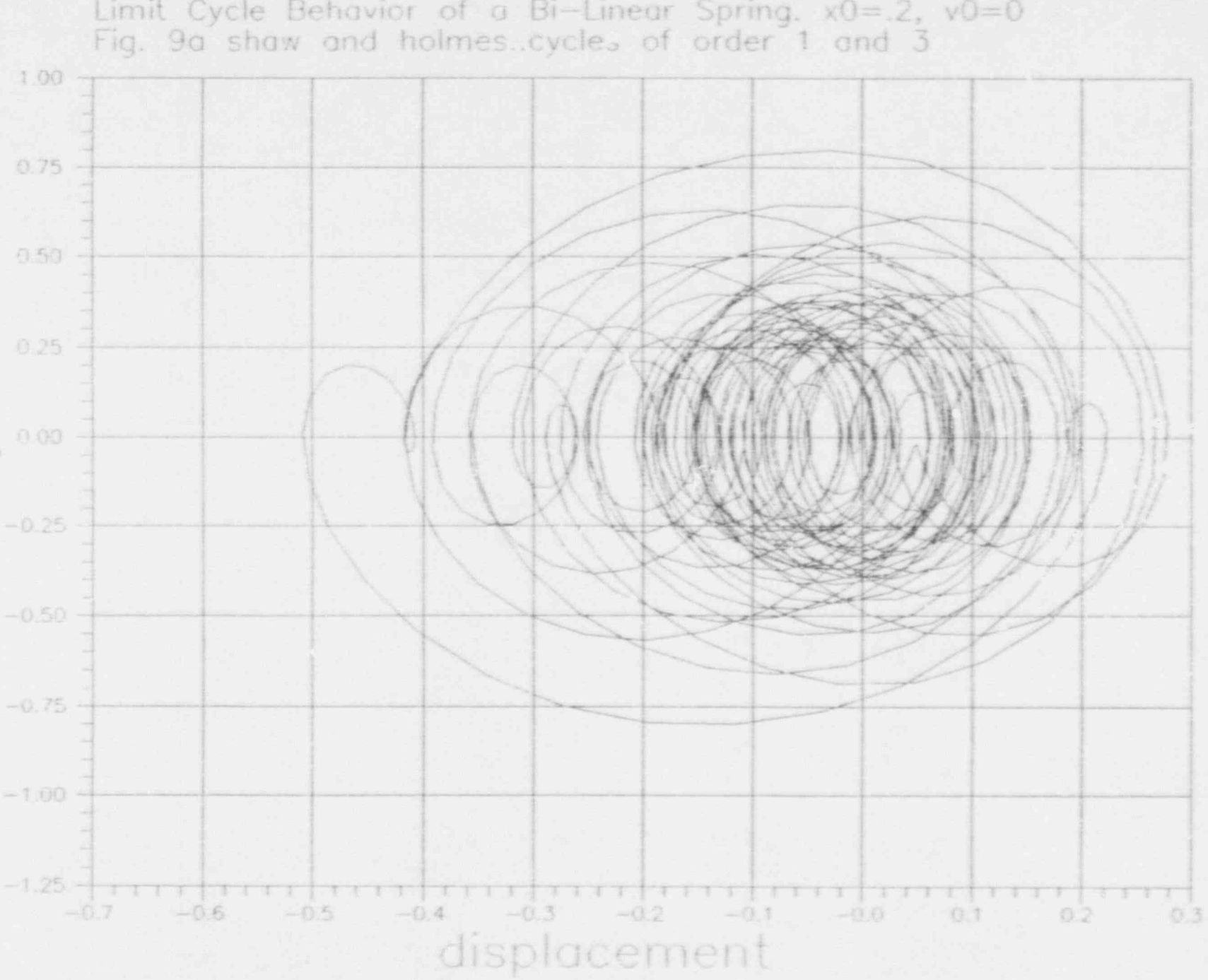
Limit Cycle Behavior of a Bi-Linear Spring. x0=.2, v0=0
Fig. 9a shaw and holmes..cycles of order 1 and 3
1.00
0.75
0.50
0.25
0.00
-0.25
-0.50
-0.75
-1.00
-1.25
velocity
-0.7
-0.6
-0.5
-0.4
-0.3
-0.2
-0.1
-0.0
0.1
0.2
0.3
displacement

FIGURE 2.13

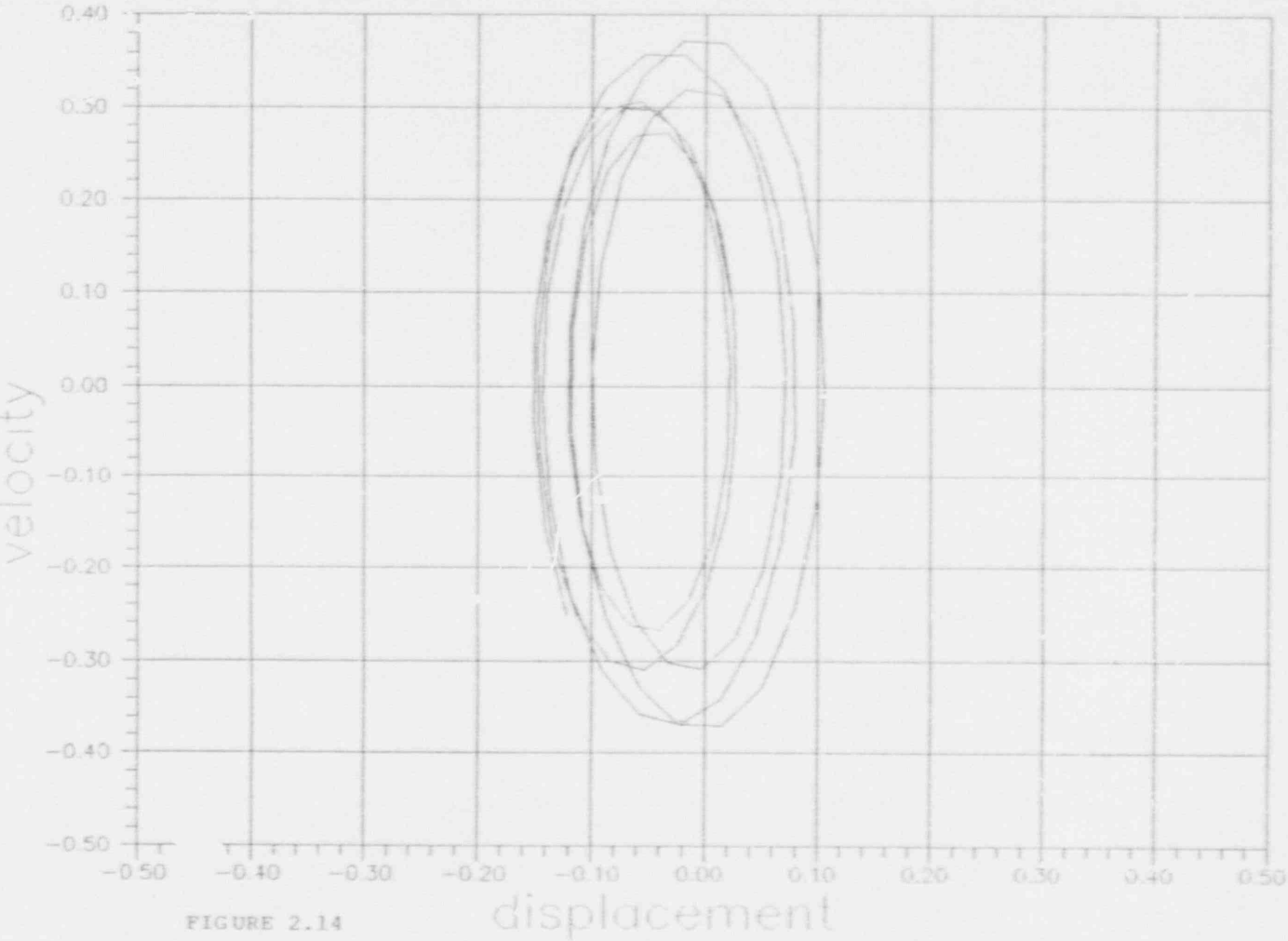
Limit Cycle Behavior of a Bi-Linear Spring. x0=.2, v0=0
Fig. 9a shaw and holmes..cycles of order 1 and 3
0.40
0.30
0.20
0.10
0.00
-0.10
-0.20
-0.30
-0.40
-0.50
velocity
-0.50
-0.40
-0.30
-0.20
-0.10
0.00
0.10
0.20
0.30
0.40
0.50
displacement

FIGURE 2.14

APPENDIX A

SEC. 2.14 From Textbook
"Component Element Method", McGraw Hill (1976)
by S. Levy and J. Wilkinson

(Subharmonic Resonance)

in the third, and 60 Hz to 120 Hz in the fourth. Let the g-level be $0{\cdot}31g$ at $t = 0$, $1{\cdot}25g$ at $t = 1{\cdot}0$, $5{\cdot}0g$ at $t = 2{\cdot}0$, $5{\cdot}0g$ at $t = 3{\cdot}0$, and $0{\cdot}0g$ at $t = 4{\cdot}0$. This description corresponds to constant displacement amplitude excitation below 30 Hz, and a roll-off to $0g$ between 60 Hz and 120 Hz.

2.46 In some cases at resonance, the forces are severe enough to cause a bolt to lift off its seat. In such a case, the effective spring stiffness drops markedly at lift-off. Rerun the example problem with $c = 0{\cdot}15$ lb sec/in. and add $k_n = -800$ lb/in., $y_n = 0{\cdot}222$ in., corresponding to lift-off at $50g$ ($900 \times 0{\cdot}222/4 = 50g$). The total stiffness after lift-off is $900 - 800 = 100$ lb/in. How does the peak amplitude compare with the value in Fig. 2.38?

2.47 Repeat problem 2.46 for decreasing frequency. (*Hint*: Let frequency be 100, 60, 30, 5 and g-level be 1, 5, 5, 1 for times 0·0, 1·0, 2·5, and 3·0, respectively.) Note the difference in response for increasing and decreasing frequency for this nonlinear system.

2.48 Repeat problems 2.46 and 2.47 with $c = 0{\cdot}20$. Does the increased damping cause a marked decrease in amplitude for this nonlinear problem?

2.14 SUBHARMONIC RESONANCE

Subharmonic resonance can occur in mechanical systems if the spring force is nonlinear. As an example, we will consider a system for which

$$\text{spring force} = 90(y - x) + 10(y - x)^2$$

We take the mass as 0·1036 lb sec^2/in., so that the low amplitude natural frequency is 4·7 Hz. The system is excited by a support movement at 9·4 Hz.

The response is shown in Fig. 2.39. The response is quite nonlinear with both $c = 0{\cdot}0$ and $c = 0{\cdot}3$; however, it is evident that the 4·7 Hz component is much larger than the 9·4 Hz component. An interesting feature of the response curves is their tendency to treat the $+5g$ level as a barrier. In the spring force sketch, we note that the maximum compressive force developed by the nonlinear spring is 202·5 lb at 4·5 in. compression. Here m represents a weight of 40 lb, so the spring can at most apply $202{\cdot}5/40 = 5{\cdot}06g$ of upward acceleration. The damper might modify this value slightly. For the spring elongation, however, the restoring force becomes quite high and results in downward accelerations as high as $15g$.

Problems

2.49 Repeat the example problem with the support g-level increased from $10g$ to $15g$.

2.50 Repeat the example problem with the exciting frequency at three times the low amplitude natural frequency.

2.51 Repeat problems 2.49 and 2.50 with $k_2 = 5$ lb/in.^{3} instead of 10 lb/in.^{3}.

2.15 SUMMARY

This chapter has concerned itself with the single mass system. In general, restoring forces of the system were nonlinear, consisting of nonlinearly hardening or softening springs, friction, or stops. Numerous examples of such systems were studied by means of a computer program given in FORTRAN in section 2.4 of this chapter. The numerical examples were designed to illustrate each feature of the computer program:

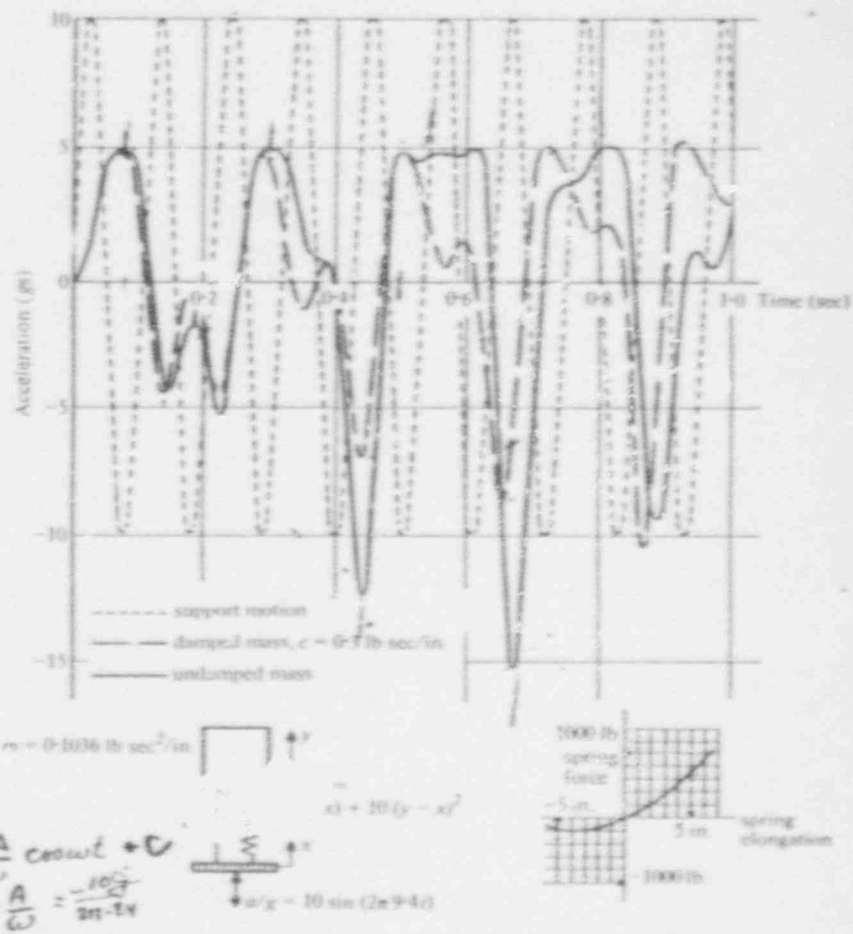

FIGURE 2.39
Response of nonlinear system with spring force = 90 (displacement) + 10 (displacement)^2 to excitation at 9·4 Hz. Low amplitude natural frequency $\omega_n = 4{\cdot}7$ Hz. Response shows subharmonic resonance effect.

namely, each element (springs of various types, stops, friction), and each type of excitation (forces on the mass, acceleration of the support, and time-varying excitations of one kind or another). In addition, we made comparisons between the numerical results of the computer program and some of the known solutions existing in the literature for nonlinear systems.

We have reached a point where we can inquire into the behavior of a system having more than one mass, each mass interacting with others by means of springs, dampers, friction, and stops. Such multi-mass systems will be discussed in the next chapter, where computer programs suitable for their study will also be given.

APPENDIX B

(SLIDING FRICTION AND DEAD BANDS)

Static and Sliding Friction in Feedback Systems

J. Tou* AND P. M. SCHULTHEISS
Department of Electrical Engineering, Yale University, New Haven, Connecticut
(Received January 16, 1953)

One of the most common nonlinearities encountered in servomechanisms design is the friction phenomenon in electromechanical systems. Conventional linear theory fails to predict its effect upon system performance. This paper extends familiar techniques to the treatment of friction nonlinearity in servosystems. Frequency-response methods are employed throughout and the theoretical results are verified by means of an analog computer. Sliding friction and static friction are represented by describing functions which form the critical factors in determining system stability. The analysis indicates that certain series equalizers designed from linear theory may fail to achieve effective compensation in the presence of sliding and static friction. On the other hand, a subsidiary loop may avoid the stability problem while still realizing an essentially equivalent loop gain function.

I. INTRODUCTION

WHILE basic analysis and synthesis procedures for linear feedback systems have become well established during the last decade, there is no correspondingly broad approach to nonlinear problems. Except in very simple cases, no general solutions are possible, and the designer must rely either on machine computation or on various linear or quasi-linear approximations. A variety of such approximations has been developed to fit numerous types of systems and successful design procedures have been discovered for a great many practical problems. It is the purpose of this paper to extend one of these techniques so as to make it applicable to the analysis of feedback systems involving sliding and static friction. Particular attention will be paid to certain loop gain functions which appear to be quite satisfactory on the basis of linear analysis but are found to be unstable in practice as a result of friction phenomena. Methods of predicting, and hence presumably preventing, such behavior will be outlined.

II. REVIEW OF BASIC PROCEDURE

The technique to be employed was first devised by Kochenburger[1] for the analysis of contractor servomechanisms and subsequently adapted for use with other nonlinear devices.[2,3] The basic procedure has been described extensively in the literature[1-4] and will therefore be outlined only briefly. It is unique in that it permits use of the frequency domain in an approach to problems involving certain types of nonlinear elements. If a sinusoidal voltage is applied to a nonlinear device, the output is generally not sinusoidal. However, under rather general conditions the fundamental component of the output will be greater than any harmonic, a difference which will be further emphasized by effective low-pass filters such as servomotors. Adequate accuracy can therefore be obtained in many cases by considering only the fundamental component of the output. Since the amplitude and phase of the fundamental component varies with the amplitude of the applied sinusoid, the approximate characteristics of the nonlinear device are represented by an "amplitude-dependent describing function" $H_a(x) = f(x)e^{j\lambda(x)}$ (see Fig. 1). If x represents the amplitude of a sinusoidal input signal, $f(x)$ is the ratio of the fundamental output to the input amplitude and $\lambda(x)$ is the phase shift of the output fundamental relative to the input signal. Note that $H_a(x)$ is frequency invariant, it depends only on the input amplitude.

Once $H_a(x)$ is known, a stability analysis can proceed essentially as in the linear case. Consider the simple loop shown in Fig. 2. System stability is governed by the roots of the equation

$$1 + H_a(x)H(s) = 0 \tag{1}$$

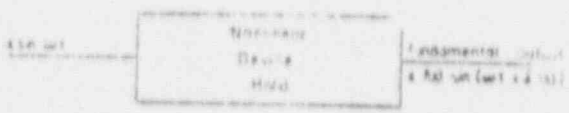

FIG. 1. Describing function of a nonlinear device.

or

$$H(s) = -1/H_a(x). \tag{2}$$

In the linear case $H_a(x) = 1$ and the stability problem reduces to the conventional one, solved easily by means of a Nyquist plot. The only modification required for the nonlinear case under the assumptions stated is a change in the critical point which now becomes $-1/H_a(x)$ instead of -1. Thus the critical point changes with the signal amplitude, and it becomes necessary to plot an amplitude locus $-1/H_a(x)$ in addition to the frequency locus $H(s)$. If the amplitude locus lies completely outside the frequency locus, the system is stable under all conditions of operation.[4] Figure 3 shows intersecting loci. Here the system is unstable for small disturbances, but stable for large disturbances so

* Now with Philco Corporation, Philadelphia, Pennsylvania.
[1] R. J. Kochenburger, Elec. Eng. 69, 687 (1950). See also Trans. Am. Inst. Elec. Engrs. 69, 270 (1950).
[2] E. C. Johnson, dissertation, Massachusetts Institute of Technology, 1951; Trans. Am. Inst. Elec. Engrs. 71I, 169 (1952).
[3] E. S. Sherrard, Trans. Am. Inst. Elec. Engrs. 71II, 112 (1952).
[4] Frequently the inverse loci, $1/H(s)$ and $-H_a(x)$, are plotted. The choice is governed simply by computational convenience in particular instances.

B2

that oscillations will tend to stabilize near the intersection point P which thus specifies the steady-state conditions, at least to a first approximation.[1]

In summary, analysis of the stability problem will require the following steps.

(a) Determination of the wave form at the output of the nonlinear device resulting from a sinusoidal input.

(b) Calculation of the describing function $H_d(x)$ from the wave shape obtained in (a).

(c) Plot and interpretation of the amplitude and frequency loci for the system under consideration. For the cases of particular interest here this step requires rearrangement of the conventional block diagram in order to secure effective separation of all transfer functions into two classes: The class of all linear but frequency sensitive components and that of all nonlinear but frequency insensitive elements.

The following definitions will be used throughout this paper. Static friction is the torque required to initiate rotation. Sliding friction is the velocity-independent component of the torque necessary to maintain such motion once started. Viscous friction is that component of the torque which is linearly proportional to the angular velocity of the rotating member.

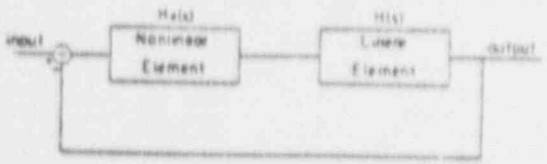

FIG. 2. Feedback loop with nonlinear element.

III. SLIDING FRICTION IN SERVOSYSTEMS

A. Wave Form Resulting from a Sinusoidal Input Torque to a System with Sliding Friction

If only sliding friction is considered the entire friction phenomenon can be represented by the characteristic curve of Fig. 4.

Consider a rotating member with moment of inertia J and angular acceleration $\ddot{\theta}$. Because of sliding friction the effective accelerating or decelerating torque τ_e is related to the applied torque τ_a through the equation

$$\tau_e = \tau_a \pm T_c, \tag{3}$$

where T_c is defined by Fig. 4. From Newton's law of motion,

$$\tau_a = T_c + J\ddot{\theta} \text{ for angular velocity } \dot{\theta} > 0 \tag{4}$$

$$\tau_a = -T_c + J\ddot{\theta} \text{ for } \dot{\theta} < 0. \tag{5}$$

From Eqs. (3), (4), and (5), the angular acceleration of the rotating member is given by

$$\ddot{\theta}(t) = \tau_e(t)/J. \tag{6}$$

Hence $\ddot{\theta}(t)$ has the same wave form as $\tau_e(t)$.

If the applied torque τ_a is sinusoidal,

$$\tau_a(t) = T_a \sin\omega t \tag{7}$$

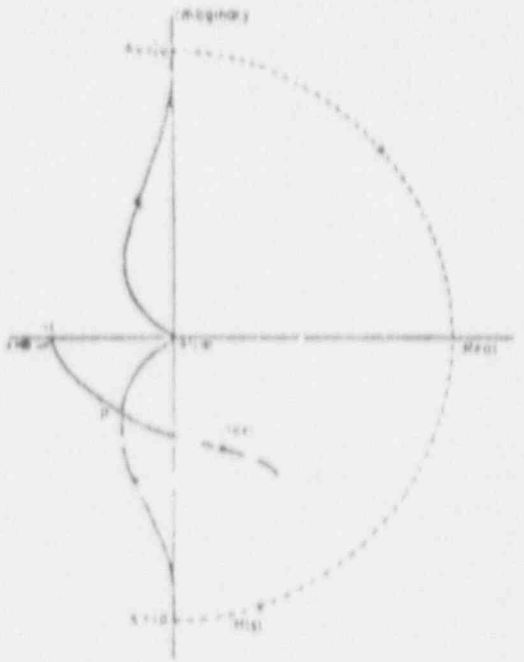

FIG. 3. Amplitude and frequency loci.

The corresponding steady-state wave forms are sketched in Figs. 5 and 6. The effective torque wave derived from eq. (3) is shown in dotted lines. The discontinuities of the τ_e wave correspond to zeros of the $\ddot{\theta}$ wave because the frictional torque T_c changes sign at those instants. On the $\dot{\theta}$ curve, point P is the point of inflection, corresponding to maximum acceleration. Since the steady state is of primary interest, the reference time is chosen after the oscillation has reached its steady-state value. $\dot{\theta}(t)$ passes through zero at

$$\omega t = n\pi = \alpha, \quad n = 0, 1, 2, 3 \cdots,$$

while

$$\tau_a = T_c \quad \text{at} \quad \omega t = \alpha.$$

FIG. 4. Sliding friction characteristic.

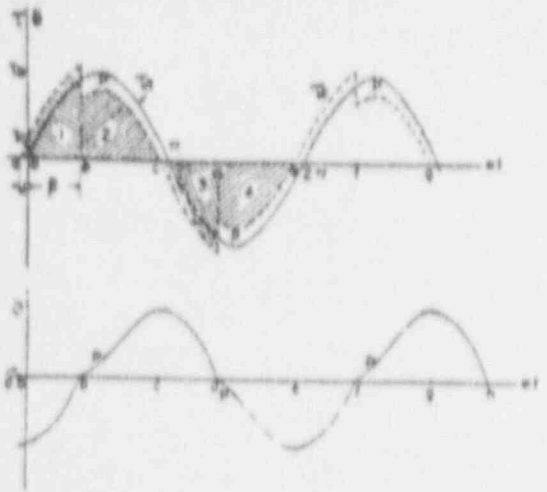

FIG. 5. Steady-state wave forms without dead zones.

It follows that

$$a = \sin^{-1}\lambda, \tag{8}$$

where

$$\lambda = T_d/T_a. \tag{9}$$

Only the angle β corresponding to the first discontinuity point remains unknown. Once it has been evaluated in terms of λ, the wave form is completely determined. There are two possibilities: If $\alpha \leq \beta$, there is no dead zone in the r_s wave (Fig. 5). If $\alpha > \beta$, there are dead zones as indicated in Fig. 6. These two cases will be considered separately.[6]

Mathematical Representation of the Steady-State Wave Forms

Case (1).—No dead zone. $\alpha \leq \beta$.

Refer to Fig. 5. In the absence of viscous friction, the following steady-state conditions exist.

Shaded area No. 1 = shaded area No. 2
= shaded area No. 3
= shaded area No. 4, etc.[6]

But between a and b,

$$r_s = T_a \sin\omega t + T_d$$
$$= T_a(\sin\omega t + \sin\alpha) = T_a(\sin\omega t + \lambda); \tag{10}$$

and between b and c,

$$r_s = T_a \sin\omega t - T_d$$
$$= T_a(\sin\omega t - \sin\alpha) = T_a(\sin\omega t - \lambda). \tag{11}$$

Then

$$\text{area No. 1} = \int_{-\alpha}^{\beta} T_a(\sin\omega t + \sin\alpha)\,d(\omega t)$$

$$= T_a(-\cos\beta + \beta\sin\alpha + \cos\alpha + \alpha\sin\alpha), \tag{12}$$

and

$$\text{area No. 2} = \int_{\beta}^{\pi-\alpha} T_a(\sin\omega t - \sin\alpha)\,d(\omega t)$$

$$= T_a[\cos\alpha - (\pi - \alpha)\sin\alpha + \cos\beta + \beta\sin\alpha]. \tag{13}$$

If Eqs. (12) and (13) are set equal and simplified, the result is

$$\cos\beta = \pi\sin\alpha/2$$

or

$$\beta = \cos^{-1}(\pi\lambda/2). \tag{14}$$

For the extreme case, $\beta = \alpha$, Eq. (14) becomes

$$\sin^{-1}\lambda = \cos^{-1}(\pi\lambda/2)$$

or

$$\lambda^2 + (\pi\lambda/2)^2 = 1.$$

A solution for λ yields

$$\lambda = \lambda_c = 0.536. \tag{15}$$

λ_c is the critical value of the quantity T_d/T_a. There is no dead zone for $\lambda \leq \lambda_c$, and there are dead zones for $\lambda > \lambda_c$.

Case (2).—With dead zones. $\alpha > \beta$.

In like manner, one obtains from Fig. 6:

shaded area No. 1 = shaded area No. 2
= shaded area No. 3
= shaded area No. 4, etc.

But, between a and b,

$$r_s = T_a(\sin\omega t + \lambda), \tag{16}$$

between b and c,

$$r_s = 0; \tag{17}$$

and between c and d,

$$r_s = T_a(\sin\omega t - \lambda). \tag{18}$$

Hence,

$$\text{area No. 1} = \int_{-\alpha}^{\beta} T_a(\sin\omega t + \lambda)\,d(\omega t)$$

$$= T_a(-\cos\beta + \beta\lambda + \cos\alpha + \alpha\lambda), \tag{19}$$

$$\text{area No. 2} = \int_{\alpha}^{\pi-\alpha} T_a(\sin\omega t - \lambda)\,d(\omega t)$$

$$= T_a[\cos\alpha - (\pi - \alpha)\lambda + \cos\alpha + \alpha\lambda]. \tag{20}$$

Equating (19) and (20) and simplifying

$$\lambda\beta - \cos\beta = (1-\lambda^2)^{\frac{1}{2}} - (\pi - \sin^{-1}\lambda)\lambda. \tag{21}$$

For the extreme case $\alpha = \beta = \sin^{-1}\lambda$,

$$\lambda\sin^{-1}\lambda - (1-\lambda^2)^{\frac{1}{2}} = (1-\lambda^2)^{\frac{1}{2}} - (\pi - \sin^{-1}\lambda)\lambda$$

or

$$\lambda = \lambda_c = 0.536 \text{ as before.} \tag{15}$$

[6] Note that a dead zone or region of zero effective torque and velocity such as *bc* on F_d, 6 occurs whenever the applied torque is smaller in magnitude than T_s at the instant when the velocity reaches zero.

[6] Velocity is proportional to the integral of torque in the absence of viscous friction.

B. Calculation of the Describing Function

Since $\tau_e(t)$ is a periodic function of time, it can be expressed in terms of a Fourier series:

$$\tau_e(t) = \frac{b_0}{2} + \sum_{n=1}^{\infty} (a_n \sin n\omega t + b_n \cos n\omega t). \tag{22}$$

It has been pointed out that, to a first approximation, $\tau_e(t)$ can be represented by the fundamental component of its Fourier series. From symmetry considerations, $b_0 = 0$. This implies oscillation about the rest position which is a condition of primary interest in stability analyses.[7] Then

$$\tau_e(t) = a_1 \sin\omega t + b_1 \cos\omega t, \tag{23}$$

where

$$a_1 = \frac{1}{\pi} \int_{t_0}^{t_0+\pi} \tau_e(t) \sin(\omega t) d(\omega t) \tag{24}$$

and

$$b_1 = \frac{1}{\pi} \int_{t_0}^{t_0+\pi} \tau_e(t) \cos(\omega t) d(\omega t). \tag{25}$$

Evaluation of the Fourier Coefficients

Case (1).—No dead zone, $\lambda \leq \lambda_0$ or $\alpha \leq \beta$.

$$a_1 = \frac{2}{\pi} \int_{-\alpha}^{\beta} T_a(\sin\omega t + \lambda) \sin(\omega t) d(\omega t) + \frac{2}{\pi} \int_{\beta}^{\pi-\alpha} T_a(\sin\omega t - \lambda) \sin(\omega t) d(\omega t) = T_a(1 - 2\lambda^2). \tag{26}$$

Similarly

$$b_1 = 2T_a\lambda[(2/\pi)^2 - \lambda^2]^{\frac{1}{2}}. \tag{27}$$

Equation (23) may also be written in the form

$$\tau_e(t) = C_1 \sin(\omega t + \delta), \tag{28}$$

where

$$C_1 = (a_1^2 + b_1^2)^{\frac{1}{2}} = T_a\left[1 - 4\left(1 - \frac{4}{\pi^2}\right)\lambda^2\right]^{\frac{1}{2}} \tag{29}$$

and

$$\delta = \tan^{-1}\frac{b_1}{a_1} = \tan^{-1}\frac{2\lambda[(2/\pi)^2 - \lambda^2]^{\frac{1}{2}}}{1 - 2\lambda^2}. \tag{30}$$

Hence, with an applied torque $\tau_e(t) = T_a \sin\omega t$, the effective torque is

$$\tau_e(t) = T_a\left[1 - 4\left(1 - \frac{4}{\pi^2}\right)\right]^{\frac{1}{2}} \times \sin\left[\omega t + \tan^{-1}\frac{2\lambda[(2/\pi)^2 - \lambda^2]^{\frac{1}{2}}}{1 - 2\lambda^2}\right]. \tag{31}$$

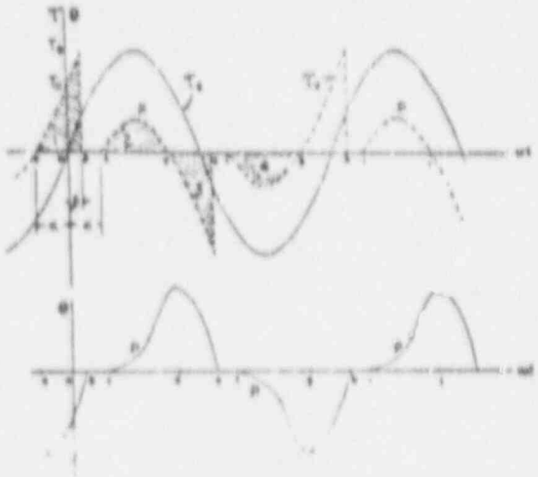

FIG. 5. Steady-state waveforms with dead zones.

In accordance with the definition of Sec. II, the describing function for the sliding-friction element is

$$H_0(\lambda) = f(\lambda) \angle \delta(\lambda) = \left[1 - 4\left(1 - \frac{4}{\pi^2}\right)\lambda^2\right]^{\frac{1}{2}} \angle \tan^{-1}\frac{2\lambda[(2/\pi)^2 - \lambda^2]^{\frac{1}{2}}}{1 - 2\lambda^2}. \tag{32}$$

Case (2).—With dead zones, $\lambda \geq \lambda_0$ or $\alpha \geq \beta$.

$$a_1 = \frac{1}{\pi} \int_{\alpha}^{\pi+\beta} T_a(\sin\omega t - \lambda) \sin(\omega t) d(\omega t) + \frac{1}{\pi} \int_{\pi+\beta}^{2\pi+\alpha} T_a(\sin\omega t + \lambda) \sin(\omega t) d(\omega t)$$

$$= (T_a/\pi)[\pi - (\alpha - \beta) - \sin\alpha(\cos\alpha + \cos\beta) - \cos\beta(\sin\alpha + \sin\beta)]. \tag{33}$$

Similarly

$$b_1 = (T_a/\pi)(\sin\alpha + \sin\beta)^2. \tag{34}$$

Hence in complete analogy with case (1) the friction-describing function is given by the expression

$$H_0(\lambda) = f(\lambda) \angle \delta(\lambda), \tag{35}$$

where

$$f(\lambda) = \frac{1}{\pi}\{[\pi - (\alpha - \beta) - \sin\alpha(\cos\alpha + \cos\beta) - \cos\beta(\sin\alpha + \sin\beta)]^2 + [(\sin\alpha + \sin\beta)^2]^2\}^{\frac{1}{2}}$$

and

$$\delta(\lambda) = \tan^{-1}\frac{(\sin\alpha + \sin\beta)^2}{\pi - (\alpha - \beta) - \sin\alpha(\cos\alpha + \cos\beta) - \cos\beta(\sin\alpha + \sin\beta)}.$$

[7] Extensions to nonzero means are possible but complicate the analysis appreciably. See reference 1.

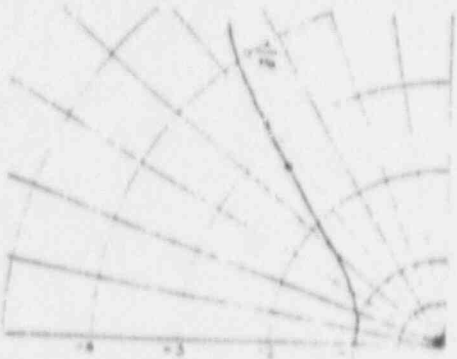

FIG. 7. The C locus.

C. C Locus

The C locus will be defined as a polar plot of the quantity $(-1/H_0)$. For any given system T_r is constant and H_0 is a function of T_a (because $T_a = T_r/\lambda$). For a fixed value of T_a, H_0 is a complex quantity which may be represented by a vector in the complex plane. The curve of $(-1/H_0)$, the C locus, forms the "critical locus" for system stability considerations, with the "critical point" $(-1, 0)$ as a special case for linear systems. The C locus is plotted in Fig. 7.

IV. SLIDING AND STATIC FRICTION IN SERVO SYSTEMS

A. Wave Form Resulting from a Sinusoidal Input Torque to a System with Sliding and Static Friction

If both sliding and static friction are considered, the friction phenomenon can be represented by the characteristic curve of Fig. 8. It will be satisfactory for most purposes to assume instantaneous transition from the static to the sliding friction value although this procedure does imply a degree of idealization.

Wave forms of $r_a(t)$ corresponding to an applied torque $r_a(t) = T_a \sin\omega t$ are easily sketched by a procedure identical with that used in Sec. III (Figs. 9 and 10). As before, there are two modes of oscillation, with and without dead zones. The latter is indistinguishable from the corresponding case discussed in Sec. III because the system is continually in motion. Thus only the former requires detailed discussion.

Mathematical Representation of the Steady-State Wave Forms

Case (1).—No dead zone, $\lambda \leq \lambda_c$, or $\alpha_1 \leq \beta$.

From Sec. III, Eqs. (10) and (11), one immediately obtains the equations for $r_a(t)$,

$$r_a(t) = T_a(\sin\omega t + \lambda) \quad \text{for} \quad -\alpha_1 \leq \omega t \leq \beta \tag{36}$$

$$r_a(t) = T_a(\sin\omega t - \lambda) \quad \text{for} \quad \beta < \omega t < \pi - \alpha_1, \tag{37}$$

where $\lambda = T_r/T_a$, $\alpha_1 = \sin^{-1}\lambda$ and $\beta = \cos^{-1}(\pi\lambda/2)$.

Case (2).—With dead zones,

$$\lambda > \lambda_c \quad \text{or} \quad \alpha_1 = \sin^{-1} T_r/T_a > \beta.$$

On Fig. 10,

shaded area No. 1

$$= \int_{\alpha_1}^{\pi-\alpha_1} T_a(\sin\omega t - \sin\alpha_1)\, d(\omega t)$$

$$= T_a[\cos\alpha_1 - (\pi - \alpha_1)\sin\alpha_1 + \cos\alpha_1 + \alpha_1 \sin\alpha_1], \tag{38}$$

shaded area No. 2

$$= \int_{-\alpha_1}^{\beta} T_a(\sin\omega t - \sin\alpha_1)\, d\omega t$$

$$= T_a[\cos\beta - (\pi + \beta)\sin\alpha_1 - \cos\alpha_1 + (\pi - \alpha_1)\sin\alpha_1]. \tag{39}$$

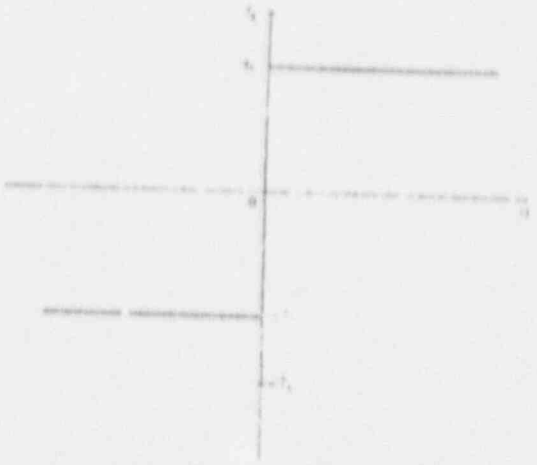

FIG. 8. Sliding and static friction characteristic.

With pure inertia load and under steady-state condition the shaded areas are equal. Equating (38) and (39) and simplifying,

$$\lambda\beta - \cos\beta = [1 - (\lambda T_r/T_a)^2]^{\frac{1}{2}} - [\pi - \sin^{-1}(\lambda T_r/T_a)\lambda]. \tag{40}$$

Equation (40) defines β in terms of known parameters. It is clear that the system will not move at all if $\lambda \geq T_a/T_r$, for then $T_r \geq T_a$.

B. Calculation of the Describing Function

Approximate expressions for effective torque are obtained by reasoning similar to that in Sec. III.

$$r_e(t) \doteq a_1 \sin\omega t + b_1 \cos\omega t, \tag{22}$$

where a_1 and b_1 are given by Eqs. (24) and (25), respectively.

Case (1).—No dead zone, $\lambda \leq \lambda_c$, $\alpha_1 \leq \beta$.

Since the equations for $r_a(t)$ are identical with those

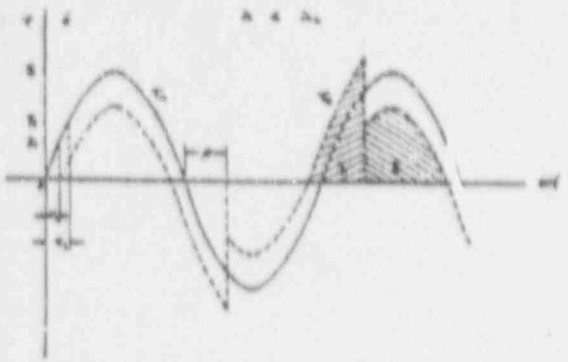

FIG. 9. Steady-state wave forms without dead zones.

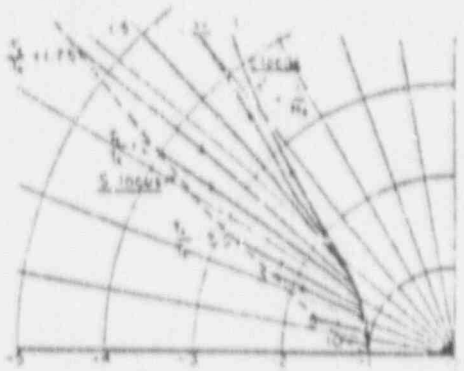

FIG. 11. Static friction loci, S locus.

in case (1) of Sec. III, the describing function $H_0(\lambda) = f(\lambda)\angle\delta(\lambda)$ is given by Eq. (32), and $f(\lambda)$ and $\delta(\lambda)$ have the following limiting values:

$$f(\lambda_s) = \frac{T_s/T_c}{[2.46+(T_s/T_c)^2]^{\frac{1}{2}}} \tag{41}$$

$$\delta(\lambda_s) = \tan^{-1}\frac{(4/\pi)(T_s/T_c)}{(\pi/2)^2+(T_s/T_c)^2-2[(\pi/2)^2+(T_s/T_c)^2]^{\frac{1}{2}}} \tag{42}$$

Case (2)—With dead zones, $\lambda \gg \lambda_s$, $\alpha_2 \gg \beta$.

$$a_1 = \frac{1}{\pi}\int_{\alpha_1}^{\pi-\beta} 2T_s(\sin\omega_1 t-\lambda)\sin(\omega_1 t)\,d(\omega_1 t)$$

$$= (T_s/\pi)[\pi-(\alpha_1-\beta)+\cos\alpha_2(\sin\alpha_2-2\sin\alpha_1) - \cos\beta(2\sin\alpha_1+\sin\beta)] \tag{43}$$

in like manner

$$b_1 = (T_s/\pi)[\sin\beta(2\sin\alpha_1+\sin\beta) + \sin\alpha_2(2\sin\alpha_1-\sin\alpha_2)]. \tag{44}$$

Hence the describing function for the static friction element is

$$H_0(\lambda) = f(\lambda)\angle\delta(\lambda),$$

where

$$f(\lambda) = \frac{1}{\pi}\{[\pi-(\alpha_1-\beta)-\cos\alpha_2(2\sin\alpha_1-\sin\alpha_2)-\cos\beta(2\sin\alpha_1+\sin\beta)]^2 + [\sin\alpha_2(2\sin\alpha_1+\sin\beta)+\sin\alpha_2(2\sin\alpha_1-\sin\alpha_2)]^2\}^{\frac{1}{2}} \tag{45}$$

and

$$\delta(\lambda) = \sin^{-1}\frac{\sin\beta(2\sin\alpha_1+\sin\beta)+\sin\alpha_2(2\sin\alpha_1-\sin\alpha_2)}{\pi-(\alpha_1-\beta)-\cos\alpha_2(2\sin\alpha_1-\sin\alpha_2)-\cos\beta(2\sin\alpha_1+\sin\beta)} \tag{46}$$

C. Static Friction-Loci and S Locus

The static friction loci are polar plots of the quantity $(-1/H_0)$ for various ratios of static friction to sliding friction. The S locus is the locus of the termini of the static friction loci. The static friction loci and the S locus are plotted in Fig. 11.

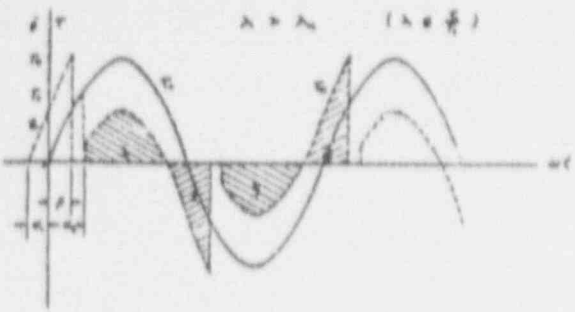

FIG. 10. Steady-state wave forms with dead zones.

V. PLOT AND INTERPRETATION OF THE AMPLITUDE AND FREQUENCY LOCI. EXAMPLES

Once the friction-describing function has been calculated, the desired stability information can be obtained easily by the method outlined in Sec. II. The procedure will be explained with the aid of a specific example which has been so chosen that a common type of corrective network will produce instability whereas another type of equalizer, apparently equivalent on a linear basis, will lead to a stable performance.

Consider the positioning loop shown in Fig. 12. In the absence of friction the loop gain function $A(s)$[4] has the form

$$A(s) = \frac{K_1}{s(1+Ts)}H_c(s), \tag{47}$$

A block diagram for this loop is shown in Fig. 13. The

[4] $A(s)$ is defined as the negative of the loop gain.

friction describing function relates applied torque to effective torque, neither of which appears as an explicit quantity in Fig. 13. This diagram therefore does not lend itself readily to the analysis of friction. However, it is easy to construct the equivalent block diagram of Fig. 14 by rearranging the basic equations describing motor performance. Torque now appears explicitly, and it is a simple matter to write the loop gain equation in terms of the friction-describing function and the system parameters defined in Fig. 12. The equation

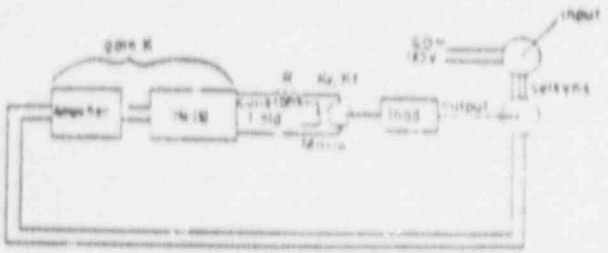

FIG. 12. Simple positioning system. $T = JR/K_sK_T$ = motor time constant; $H_s(s)$ = equalizer transfer function; K_T = motor torque per unit armature current; K_s = motor counter emf per unit speed; J = motor and load inertia; K_1 = gain of amplifier and selsyn $= K_iK_s$; R = armature loop resistance.

has the form

$$A(s) = H_0(\lambda)\frac{K_T}{Js^2}\left[\frac{K_s s}{R} + \frac{K_T}{R}H_s(s)\right]. \tag{48}$$

Note that viscous damping due to counter emf is represented by the additional feedback path rather than the conventional velocity-dependent load on the output member. This step is necessary because the friction-describing function was derived for the case of a pure inertia load. The procedure is obviously based on the assumption that a sinusoid applied to the nonlinear

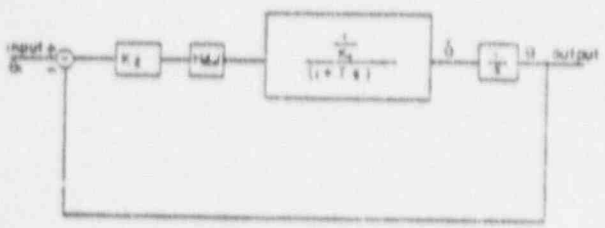

FIG. 13. Conventional block diagram.

device yields an output signal of which only the fundamental is significant in transmission around each loop, so that only sinusoids of the same frequency need be considered. This assumption becomes progressively poorer as damping, and hence the interior loop gain, increases. However, it will be seen that the method still leads to acceptable first approximations in cases of considerable practical interest.

Consider the system of Fig. 12 with the following arbitrary numerical parameters, all given in a consistent set of units.

$$K_T = K_s = 0.1, \quad R = 1, \quad J = 0.001, \quad K_1 = 500, \quad K_2 = 50, \quad T = 0.1. \tag{49}$$

Equation (47) now becomes

$$A(s) = \frac{500}{s(1+0.1s)}H_s(s). \tag{50}$$

In the absence of an equalizer $H_s(s)$ the loop would be close to instability. Let $H_s(s)$ be a two stage lag network or integral equalizer

$$H_s(s) = \left(\frac{1+0.3s}{1+3s}\right)^2. \tag{51}$$

Without friction the system would exhibit a phase margin of 26° and a fairly well-damped transient response. The Nyquist diagram of Fig. 15 confirms that deduction. Note, however, that the sliding friction (C) locus intersects the Nyquist plot at two points. The system is evidently stable for exceedingly small disturbances; it becomes unstable as soon as a significant input signal is applied and then sustains oscillations at an amplitude

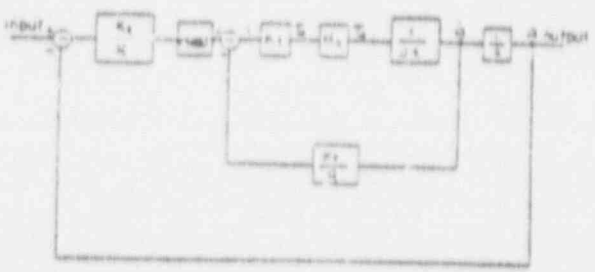

FIG. 14. Equivalent block diagram.

and frequency determined by the intersection point closer to the origin. An experimental check by analog computer resulted in oscillation at 1.6 rad/sec as compared to a theoretical value of about 2 rad/sec.

If a mino, loop is used in place of the series equalizer (Fig. 16), the result is quite different. By a process entirely equivalent to that used in rearranging the block diagram of Fig. 13 the loop gain function may be written in the equivalent form

$$A(s) = H_0(\lambda)\frac{K_T}{Js}\left[\frac{K_s + H_s(s)}{R} + \frac{K_1}{Rs}\right] \tag{52}$$

Using the equalizer transfer function[18]

$$H_s(s) = \frac{(5s)^2(1+0.1s)}{10(1+0.5s)^2(1+0.003s)} \tag{53}$$

[17] A more elaborate equalizer would probably be used in practice. This primitive form was chosen because it illustrates clearly the difficulties encountered because of friction effects.

[18] $H_s(s)$ has been chosen so as to yield a system with transfer from input to output as close as practical to the series equalized structure. Without the last denominator term (required for realizability) the two would be almost identical in the absence of friction. As it is, the step function responses are virtually indistinguishable.

and the same numerical values as in the previous case one obtains the Nyquist diagram shown along with the series equalizer case in Fig. 15. The plot does not intersect the C locus so that the system remains stable in the presence of friction. Measured results from an analog computer bear out this conclusion.

The equalizer used in the above example introduced attenuation with the third power of frequency over a 10:1 frequency range, so that the resultant frictionless system is conditionally stable. It may therefore not appear surprising that oscillations should develop when a nonlinear element is introduced into the loop. Similar results can, however, be obtained with a single stage lag network and a resultant loop of absolute stability. Consider the series equalizer

$$H(s) = (1+0.25s)/(1+10s). \tag{54}$$

The gain factor K_3 is chosen as 100, all other parameters remain unchanged from the previous example. Figure 17

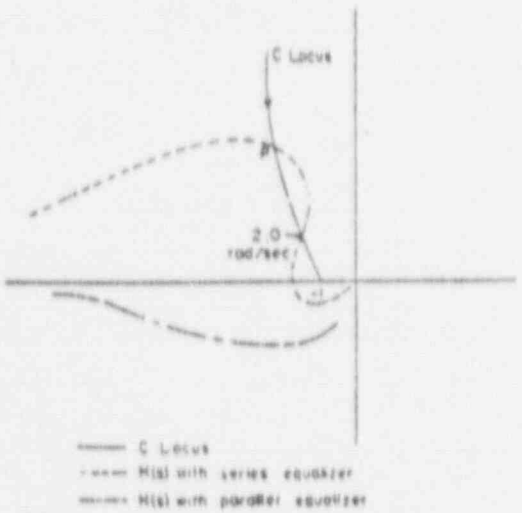

FIG. 15. Rough sketch of amplitude and frequency loci. Intersection at P is actually at a far greater distance from the origin.

shows the Nyquist plot as well as the curve for a corresponding minor loop structure. The latter is clearly stable. The Nyquist plot for the series equalizer case shows no intersection with the C locus and measurements in the presence of sliding friction alone indicate stability. However, the Nyquist diagram does cross the S locus twice, indicating that oscillations may occur when static as well as sliding friction is considered. Since the S locus traces the termini of the describing functions for various static-to-sliding-friction ratios, it is evident that stability depends critically on that ratio: only for values between those corresponding to the two intersection points can oscillations exist. It is also evident that the frequency of oscillations should rise from a theoretical minimum of 0.7 rad/sec to a maximum of 2.25 rad/sec. The corresponding range from computer measurement is 0.8 rad/sec to 2.0 rad/sec. The experimental correlation at intermediate values of the static-to-sliding friction ratio is about equally close so that the method may be said to yield a reasonable first approximation.

VI. CONCLUSIONS

The describing function technique has been extended to cover problems of static and sliding friction in feedback systems. Under certain assumptions the stability problem can be handled adequately, and the frequency

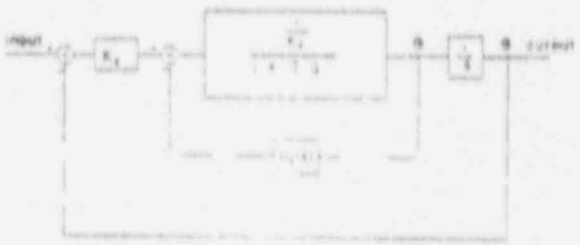

FIG. 16. Block diagram with minor loop (parallel equalizer).

of any sustained oscillations can be predicted to a first approximation. In particular it has been shown that the use of integral equalization in series with the loop may easily lead to instability when friction phenomena are important. Essentially equivalent minor loop equalizers may yield an entirely satisfactory system.

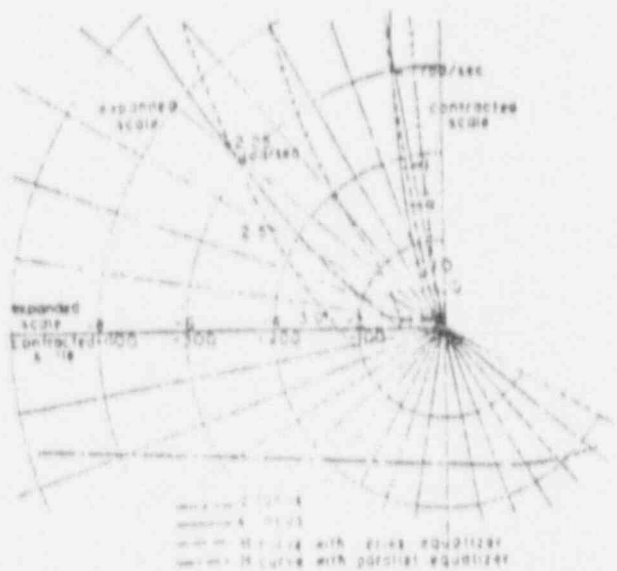

FIG. 17. Amplitude and frequency loci for an experimental system.

VII. ACKNOWLEDGMENT

The authors wish to acknowledge the aid of various members of the Electrical Engineering Department of Yale University, especially that of Professor F. B. Tuteur of the servomechanisms laboratory. The contents of this paper are taken in essence from a dissertation by Julius Tou presented to the faculty of the Yale School of Engineering in partial fulfilment of the requirements for the degree of Doctor of Engineering.

APPENDIX C

JUMP PHENOMENA

(MATHCAD SOLUTION)

CALCULATION OF HARDENING SPRING RESPONSE CURVE
Ref. Asymptotic Methods in the Theory of Non Linear Oscillations
by N.N Bogoliubov and Y.A. Mitropolsky. (U.of.Pa. Math/Physics)
Hindustan Publishing, 1961.

Theory....For assumed amplitudes, find frequencies

$a := 1.5$ $\delta := .2$ $E_1 := 1$

$\omega_e := 1 + .375\, a^2$

$$X := \left[\frac{E_1}{a}\right]^2 - \delta^2$$

$$N_1 := \sqrt{\omega_e^2 - \sqrt{X}} \qquad N_2 := \sqrt{\omega_e^2 + \sqrt{X}}$$

$N_1 = 1.662$ $N_2 = 2.009$

C2

Table C-1

NONLINEAR RESONANCE CURVE

$\bar{a}$	μ_1	μ_2
1	1.694	.954
1.1	1.732	1.101
1.05	1.711	1.033
.5	1.785	IMAGINARY
.6	1.715	IMAGINARY
.4	1.901	IMAGINARY
.3	2.097	IMAGINARY
.7	1.678	IMAGINARY
.8	1.665	.551
.75	1.669	.305
.704015078	1.677	.062
1.2	1.703	1.25
1.029	1.704	1.0
1.5	2.009	1.662
2	2.59	2.407
2.3	3.048	2.918
2.5	3.395	3.292
2.8	3.977	3.902
5.0	10.375	10.375

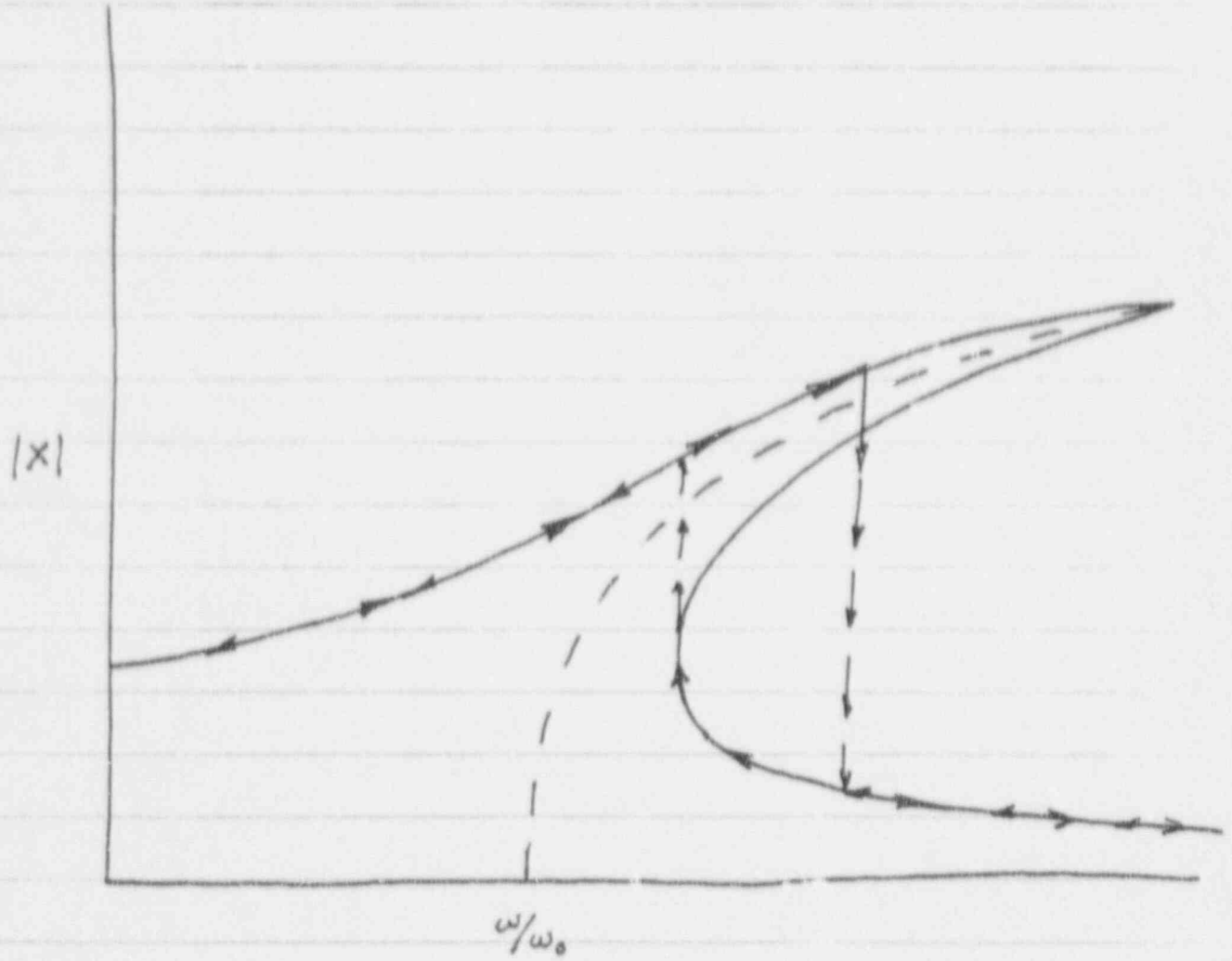

FIGURE C-1 RESONANCE CURVE SHOWING JUMP PHENOMENA